

Ionization chemistry in the inner disc: a combined treatment of ionic and thermionic emission and arbitrary grain size distributions

Morgan Williams^{1*} and Subhanjoy Mohanty¹

¹*Astrophysics Group, Imperial College London, Blackett Laboratory, Prince Consort Road, London SW7 2AZ, UK*

Accepted XXX. Received YYY; in original form ZZZ

ABSTRACT

In the inner regions of protoplanetary discs, ionization chemistry controls the fluid viscosity, and is thus key to understanding various accretion, outflow and planet formation processes. The ionization is driven by thermal and non-thermal processes in the gas-phase, as well as by dust–gas interactions that lead to grain charging and ionic and thermionic emission from grain surfaces. The latter dust–gas interactions are moreover a strong function of the grain size distribution. However, analyses of chemical networks that include ionic/thermionic emission have so far only considered grains of a single size (or only approximately treated the effects of a size distribution), while analyses that include a distribution of grain sizes have ignored ionic/thermionic emission. Here, we: (1) investigate a general chemical network, widely applicable in inner disc regions, that includes gas-phase reactions, ionic and thermionic emission, *and* an arbitrary grain size distribution; (2) present a numerical method to solve this network in equilibrium; and (3) elucidate a general method to estimate the chemical time-scale. We show that: (a) approximating a grain size distribution by an “effective dust-to-gas ratio” (as done in previous work) can predict significantly inaccurate grain charges; and (b) grain charging significantly alters grain collisional time-scales in the inner disc. For conditions generally found in the inner disc, this work facilitates: (i) calculation of fluid resistivities and viscosity; and (ii) inclusion of the effect of grain charging on grain fragmentation and coagulation (a critical effect that is often ignored).

Key words: accretion, accretion discs – astrochemistry – MHD

1 INTRODUCTION

Magnetic effects are thought to play a crucial role in driving accretion and outflow in protoplanetary discs. These effects include, e.g., the magnetorotational instability (MRI; Balbus & Hawley 1991) and magneto-hydrodynamical (MHD) winds (Blandford & Payne 1982). To be efficient, these phenomena require sufficient coupling between the magnetic field and the fluid.

The degree of field-fluid coupling is determined by the resistivities of the fluid (e.g. Gammie 1996; Jin 1996; Fleming et al. 2000; Sano & Stone 2002; Bai & Stone 2011). The resistivities in turn are set by the disc ionization chemistry, driven by various thermal and non-thermal processes. In models of protoplanetary discs, the chemistry is usually investigated via a specified chemical network. Over the past several decades, networks of increasing complexity have been developed to better represent reality. Initial networks omitted dust grains, assuming that grains would settle to the mid-plane and hence be irrelevant for studying the layered accretion model (e.g., Gammie 1996). More complete subsequent networks accounted for grains with gas–grain and grain–grain interactions, and also included a range of non-thermal ionization sources and intricate gas phase reactions, including charge transfer between species (e.g., Ilgner & Nelson 2006; Bai & Goodman 2009).

Due to computational constraints, time-dependent chemical reaction networks, such as those of Ilgner & Nelson (2006), usually

involve a single grain size with a limited set of charge states or assume a steady-state distribution of possible charges for each grain size bin (Balduin et al. 2023). Conversely, time-independent (kinetic equilibrium) chemical networks typically do include a distribution of grain sizes with a full range of possible charge states. Such networks have been used for calculations specialized to the cool outer disc (Okuzumi 2009; Fujii et al. 2011; Dzyurkevich et al. 2013; Mori & Okuzumi 2016; Ivlev et al. 2016; Marchand et al. 2021), with no thermal ionization. Marchand et al. (2022) later performed similar calculations including the effects of thermal ionization.

Meanwhile, our understanding of grain effects on the ionization has also evolved (e.g. Desch & Turner 2015; Thi et al. 2019). Earlier works (e.g., Sano et al. 2000; Ilgner & Nelson 2006; Wardle 2007; Salmeron & Wardle 2008; Bai & Goodman 2009; Mohanty et al. 2013) assumed that grains act only to reduce the ionization state of the gas, by adsorbing free charges from the gas and allowing recombinations on their surfaces. As Desch & Turner (2015) showed, this is not always true for conditions prevalent in the inner disc (≥ 800 K): grains can also *increase* the number density of free charges in the gas phase, due to thermionic and ion emission (emission of electrons and ions respectively from grains, following grain surface-catalysed ionization of alkali atoms condensed onto grains).

However, the equilibrium chemical network Desch & Turner (2015) solved only included a single grain size, with a single value of charge. Jankovic et al. (2021) extended this to a distribution of grain sizes in a simplified fashion, by combining a single grain size with an “effective” dust-to-gas ratio (motivated by earlier work by Bai &

* E-mail: m.williams22@imperial.ac.uk (MW)

Goodman 2009). As we show here (Appendix D), however, while this technique gives acceptable results for gas-phase charge densities (and thus resistivities), the grain charges it predicts are inaccurate. This is important because grain charges are vital for correctly computing grain–grain collision rates, and thus fragmentation and coagulation rates (Okuzumi 2009; Okuzumi et al. 2011a,b; Akimkin et al. 2020, 2023), which determine the grain size distribution itself in dynamical calculations. This size distribution in turn controls key aspects of disc physics: not only the (gas-phase) charge densities and thus resistivities discussed here, but also the disc opacity (e.g., Draine 2016) and the coupled dynamics of dust and gas.

To summarize: currently, disc equilibrium chemical networks that rigorously treat a distribution of grain sizes do not yet include ionic and thermionic emission from grains (e.g., Marchand et al. 2022), while equilibrium networks that do include the latter effects either do not include a grain size distribution or only treat it approximately (e.g., Desch & Turner 2015; Jankovic et al. 2021).¹

Our goal here is to redress this lack for inner disc equilibrium chemical networks. Specifically, we present a numerical method to *exactly* solve (to numerical precision) a generalized equilibrium chemical network that is widely applicable in inner disc conditions, which includes: (i) thermal and non-thermal ionization processes; (ii) ionic and thermionic emission; and (iii) an arbitrary distribution of grain sizes, with size-dependent grain charges.

Our chemical network (see Section 2) is the same as in Desch & Turner (2015), except generalized to include a distribution of grain sizes and charges. Our solution technique (Subsection 2.3) is similar to that of Marchand et al. (2022), generalized to include ionic and thermionic emission.

In section Section 2 below, we introduce our chemical network. In Section Section 3, we discuss the results of our simulations. Specifically, we: validate the results of simulation against earlier work in relevant limits (Subsection 3.1); discuss the behaviour of the full network (Subsection 3.2); investigate the distribution of charge as a function of grain size (Subsection 3.3); analyse the effect of MRN grain-size distributions with various slopes (Subsection 3.4); analyse an illustrative arbitrary (non-MRN) grain size distribution (Subsection 3.5); determine the applicability of chemical equilibrium (Subsection 3.6); and compute resistivities using our network (Subsection 3.7). Finally, our conclusions are presented in Section 4.

2 CHEMICAL NETWORK

The network we have used is an adaptation of the network employed by Desch & Turner (2015), consisting of ODEs for:

- electrons (n_e);
- a molecular ion species (n_{m^+}), produced through non-thermal ionization alone;
- a metal ion species (n_{M^+}), produced by charge transfer to a neutral metal atom from the molecular ion;
- a neutral alkali species (n_{alk^0}) which is converted to the alkali ion (n_{alk^+}) by thermal processes only;

¹ As an aside, the time-dependent network (albeit with a steady-state charge distribution in each grain size bin) of Balduin et al. (2023), that includes a distribution of grain sizes, and accounts for thermionic emission and charge exchange between ions/neutrals and grains (including for alkalis), does not account for condensation, assuming ions and neutral to be freely available in the gas-phase. As such, it also does not account for ionic emission.

- a phase of the alkali species (both neutral and ionic) condensed onto the grain surface, with a separate ODE for each grain bin (i.e., $n_{\text{alk cond}}^i$ for the i th grain size bin); and
- the charge on each grain size bin (Z^i).

We also have the equation of charge conservation. Differences with respect to the Desch & Turner (2015) network are the separate ODEs for the condensed alkali and grain charge for each grain size bin, and the inclusion of the intermediate molecular ion species.

2.1 Gas phase chemistry

2.1.1 Non-thermal ionization and downstream processes

Non-thermal ionization of H_2 occurs at a volumetric rate ζn_{H_2} . The non-thermal ionization rate of H_2 includes terms due to ionization by radionuclides, cosmic rays and high energy stellar irradiation. The ionization rate of H_2 due to radionuclides in discs is $\zeta \approx 7.6 \times 10^{-19}$ (Umebayashi & Nakano 2009), the largest contributor being the decay of ^{26}Al . This study will focus on conditions applicable to the inner-disc mid-plane; therefore, we assume that any cosmic rays or high energy stellar irradiation are shielded by the large column depths. We thus use $\zeta = 7.6 \times 10^{-19}$ in all our simulations.

In our model, through charge transfer to molecules, non-thermal ionization of H_2 results in an identical volumetric production rate of molecular ions m^+ . For definiteness, we use the molecular ion HCO^+ in all subsequent simulations. We assume that the abundance of CO, from which this ion is formed, is sufficiently high to allow rapid production of HCO^+ through charge transfer. Our simulations show low abundances of HCO^+ , indicating minimal depletion of CO. Coupled with the high abundance of CO, this supports our assumption.

The cations immediately produced by non-thermal ionization of H_2 are H_2^+ or H^+ . Before reaching neutral metal atoms M^0 , e.g., Mg, Na, Ca, Fe (Oppenheimer & Dalgarno 1974), the positive charge on these cations must be transferred, via reactions with neighbouring neutral molecular species, to form molecular ions, e.g., H_3^+ , H_2O^+ , HCO^+ (e.g. Oppenheimer & Dalgarno 1974); these molecular ions may then transfer their charge to a neutral metal atom, forming M^+ . However, the molecular ions in the chain may instead recombine, radiatively or dissociatively, meaning that the complete charge transfer from H_2^+ or H^+ to produce a metal ion M^+ is not 100% efficient. The metal ion that we use in this work is Mg^+ , due to the high abundance of Mg, $x_{\text{Mg}} = 3.67 \times 10^{-5}$ (Asplund et al. 2009).²

Charge may transfer from a molecular ion m^+ to a metal atom M^0 at a rate

$$\mathcal{R}_{\text{ct}} = \beta n_{m^+} n_{M^0} = \beta n_{m^+} (n_{M^{\text{tot}}} - n_{M^+}) \quad , \quad (1)$$

where $\beta = 3 \times 10^{-9} \text{ cm}^3 \text{ s}^{-1}$ (Oppenheimer & Dalgarno 1974) and $n_{M^{\text{tot}}}$ is the total number density of M atoms and ions. The UMIST (Millar et al. 2024) value for this rate constant for Mg^+ and HCO^+ agrees with the Oppenheimer & Dalgarno (1974) value to

² Asplund et al. (2009) in fact provides logarithmic abundances in the form $X_i = \log_{10}(n_i/n_{\text{H}}) + 12$, where X_{H} is defined to be 12. Thus, to compute $x_i = n_i / (\sum_j n_j)$ from these values, one must compute $x_i = 10^{X_i} / (\sum_j 10^{X_j})$. As done in Jankovic et al. (2021), to convert from this abundance to number density of a species i , we use $n_i^{\text{tot}} = \frac{2x_i}{2-x_{\text{H}}} \frac{\rho}{\mu_{\text{MH}}}$, where $x_{\text{H}} = 9.21 \times 10^{-1}$ (Asplund et al. 2009), ρ is the gas density and μ is the mean molecular weight, taken to be 2.34. The number density of H_2 is $n_{\text{H}_2} = \frac{x_{\text{H}}}{2-x_{\text{H}}} \frac{\rho}{\mu_{\text{MH}}}$.

within the defined accuracy. Alternatively, the molecular ion (m^+) may recombine dissociatively at a rate:

$$\mathcal{R}_{\text{diss-rec}} = \alpha n_{m^+} n_e, \quad (2)$$

where $\alpha = 3 \times 10^{-6} T^{-1/2} \text{cm}^3 \text{s}^{-1}$ (Oppenheimer & Dalgarno 1974). The UMIST (Millar et al. 2024) value for this rate constant for HCO^+ is valid only over the range 10-300 K. Therefore, we use the Oppenheimer & Dalgarno (1974) value. The molecular ion may also collide with dust grains, where it is assumed that the molecular ions gain an electron from the grains due to the ionization potential of the ion being larger than the work function of the grains. This means that electrons associated with the grains fall into the deeper potential well of the molecular ion, neutralizing it, before the neutral molecule is eventually re-emitted to the gas phase.

Once produced, the metal ions M^+ recombine radiatively at a rate given by:

$$\mathcal{R}_{\text{gas, 2-rec, } M^+} = \gamma n_e n_{M^+}, \quad (3)$$

where $\gamma = 3 \times 10^{-11} T^{-1/2} \text{cm}^3 \text{s}^{-1}$ (Oppenheimer & Dalgarno 1974). Similarly to the case for dissociative recombination, the UMIST (Millar et al. 2024) value for this rate constant for Mg^+ is defined over a subset of our desired temperature range (10-1000 K). For this reason, and to mirror the choice of (Desch & Turner 2015), allowing for direct comparison with their work, we again use the Oppenheimer & Dalgarno (1974) value.

Just like the molecular ions, metal ions also collide with dust grains and are assumed to be neutralized and re-emitted as neutral atoms.

2.1.2 Thermal Ionization and Downstream Processes

The alkali ion species alk^+ is produced by thermal processes alone; this includes collisional ionization in the gas phase and ion emission from the dust grains (see 2.2). Collisional ionization has a rate

$$\mathcal{R}_{\text{gas, coll-ion}} = k_2 n_{\text{H}_2} n_{\text{alk}^0}, \quad (4)$$

where k_2 is the rate constant. Following Desch & Turner (2015), we take the experimentally computed value (Ashton & Hayhurst 1973) $k_2 = 9.9 \pm 2.7 \times 10^{-9} T^{1/2} \exp(-\frac{IP}{kT}) \text{cm}^3 \text{s}^{-1}$ with T in units of K (while noting the discrepancy with the theoretical value from Pneman & Mitchell (1965), for which no calculation or references are provided). See Marchand et al. (2022) for a discussion of the implications of using the experimental value in place of the theoretical value. However, note that the value chosen is relatively unimportant as grain-phase ionization and emission dominate the rate of thermal production of alkali ions and electrons in the gas-phase (Desch & Turner 2015, as well as our results, shown further along).

The specific alkali adopted in this work is potassium. The reasons for this, in terms of the ionization fractions produced by different alkalis versus the threshold ionization fractions required for MRI activity (which is widely assumed to be the source of viscosity in the inner disc), are provided in Appendix A. However, for completeness, we also show in Appendix B the effect of including sodium alongside potassium in our network. While sodium is harder to ionize than potassium, it is over an order of magnitude more abundant. Hence sodium ionization dominates at the highest temperatures (although efficient MRI is possibly already assured by potassium ionization alone).

The alkali species may recombine radiatively; the equation for this

process is identical to equation 3, except with the substitution of alk^+ for M^+ .

$$\mathcal{R}_{\text{gas, 2-rec, alk}^+} = \gamma n_e n_{\text{alk}^+}. \quad (5)$$

For the same reasons as earlier, we use the value of γ from Oppenheimer & Dalgarno (1974). Alternatively to the two-body process, the alkali may recombine through a three-body process, at a rate

$$\mathcal{R}_{\text{gas, 3-rec, alk}^+} = k_{-2} n_{\text{H}_2} n_e n_{\text{alk}^+}, \quad (6)$$

where $k_{-2} = 4.4 \pm 1.1 \times 10^{-24} T^{-1} \text{cm}^6 \text{s}^{-1}$ (Ashton & Hayhurst 1973) with T in units of K.³ Three-body recombination dominates over the two-body radiative recombination at lower temperature and higher density but we include both processes in our calculations.

The neutral alkali species, alk^0 , and alkali ion species, alk^+ , may be adsorbed by grains; adsorption by grains in the i th grain size bin gives a number density $n_{\text{alk cond}}^i$. Whether the condensed species is re-emitted to the gas phase as alk^0 or alk^+ depends on the effective work function of the grains and the temperature (see 2.2).

2.2 Grain phase chemistry

Our network includes spherical dust grains, with a distribution of N sizes, with a single value of charge for each grain size. The spherical approximation is necessary for dust-phase chemistry as this requires the computation of an electrostatic potential of the grain, for which only the sphere has an analytic form.⁴ The number density of grains of size a^i is n_{gr}^i . The charge on grains of size a^i is Z^i . The total number density of grains is $n_{\text{gr}}^{\text{tot}} = \sum_{i=1}^{N_{\text{gr}}} n_{\text{gr}}^i$ (in the remainder of this work we omit the limits on sums over the grain size distribution for brevity). We will consider both arbitrary distributions of grain sizes, as well as standard MRN distributions of grain sizes (Mathis et al. 1977).

For an MRN distribution, the number density of grains in range $[a, a + da]$ is $(dn/da)da = Aa^{-q} da$. The normalization constant A is determined by the integral $\int_{a_{\text{min}}}^{a_{\text{max}}} m(a)(dn/da)da = f_{\text{dg}}\rho$, where a_{min} and a_{max} are the minimum and maximum grain size respectively, $m(a)$ is the mass of the grains ($= \frac{4\pi}{3}\rho_{\text{gr}}a^3$, where ρ_{gr} is the bulk density of the grains), f_{dg} is the dust-to-gas ratio and ρ is the gas density. Performing the above integral, we obtain:

$$A = \begin{cases} \frac{f_{\text{dg}}\rho}{\rho_{\text{gr}}} \left(\frac{1}{4\pi/3}\right) (4-q) \left(\frac{1}{a_{\text{max}}^{4-q}} - \frac{1}{a_{\text{min}}^{4-q}}\right) & \text{if } q \neq 4 \\ \frac{f_{\text{dg}}\rho}{\rho_{\text{gr}}} \left(\frac{1}{4\pi/3}\right) \left(\frac{1}{\ln(a_{\text{max}}/a_{\text{min}})}\right) & \text{if } q = 4 \end{cases}. \quad (7)$$

In this work, we assume a minimum grain size $a_{\text{min}} = 10^{-5} \text{cm}$, a maximum grain size $a_{\text{max}} = 10^{-1} \text{cm}$ and a fiducial $q = 3.5$. To fix the normalization A , we use: a dust-to-gas ratio $f_{\text{dg}} = 10^{-2}$; a bulk density for the grains of $\rho_{\text{gr}} = 3.3 \text{g cm}^{-3}$, corresponding to silicates (though this could be extended to account for compositional changes or porosity); and density $\rho = \mu m_{\text{H}} \left(\frac{2-x_{\text{H}}}{x_{\text{H}}}\right) n_{\text{H}_2}$ ($\rho \approx \mu m_{\text{H}} n_{\text{H}_2}$), where $n_{\text{H}_2} = 10^{14} \text{g cm}^{-3}$.

³ The rate constant is denoted k_{-2} as this process is the inverse of collisional ionization (equation 4), for which the rate constant is denoted k_2 .

⁴ However, we note experimental investigations indicate a fractal dimension $D \sim 2$ to be more realistic (e.g. Wurm & Blum 1998) and that the fractal dimension changes during coagulation (Okuzumi 2009). We eschew this complication here.

Dust grains adsorb gas phase species. The adsorption of species x by grains of size a^i and charge Z^i occurs with rate

$$\mathcal{R}_{x, \text{ads}}^i(Z^i) = n_x n_{\text{gr}}^i \pi (a^i)^2 \left(\frac{8kT}{\pi m_x} \right)^{1/2} S_x \bar{J}_x(Z^i e/q_x) = n_x v_x^i, \quad (8)$$

where n_x is the number density of species x in the gas phase, m_x is the mass of species x , S_x is the sticking coefficient of species x , $\bar{J}_x(Z^i e/q_x)$ is the focusing factor for species x , of charge q_x , providing the enhancement to the geometrical collision cross-section (Draine & Sutin 1987) and e is the elementary charge. We take the sticking coefficient of electrons S_e to be 0.6 and the sticking coefficient of ions and neutrals to be unity (Desch & Turner 2015; Jankovic et al. 2021). An exact calculation of the electron sticking coefficient was performed by Bai (2011) and is broadly consistent with our choice.

The adsorption of alk^0 and alk^+ by grains with size a^i gives a number density of condensed alk, $n_{\text{alk cond}}^i$. The condensed alk vibrate on the grain lattice; the frequency of this vibration is taken to be the same value as Desch & Turner (2015) used for the vibration of K on Pt of $\nu = 3.7 \times 10^{13} \text{ s}^{-1}$ (Hagström et al. 2000). The vibration cycle has a probability $\exp(-\frac{E_a}{kT})$ of resulting in evaporation of alk (Desch & Turner 2015), where E_a is the activation energy. This results in a rate of evaporation of alk from grains of size a^i :

$$\mathcal{R}_{\text{alk evap}}^i = n_{\text{alk cond}}^i \nu \exp\left(-\frac{E_a}{kT}\right) = n_{\text{alk cond}}^i \nu_{\text{evap}}. \quad (9)$$

We follow Desch & Turner (2015) in setting the activation energy to 3.25 eV, and refer the reader to Desch & Turner (2015) for a discussion of how this value was calculated.

The fraction of the alkali species alk emitted from the grains as ions (alk^+) is given by the Saha–Langmuir equation (Desch & Turner 2015) as

$$f_+^i = \frac{1}{1 + \frac{g_0}{g_+} \exp\left(-\frac{IP - W_{\text{eff}}^i}{kT}\right)}, \quad (10)$$

where W_{eff} is the effective work function of the grains. The effective work function is defined as $W_{\text{eff}} = W - e\phi$, where W is the work function and ϕ is the electrostatic potential of the grain. For spherical grains of size a , $\phi = -Ze/a$. We follow Desch & Turner (2015) and take $W = 5.0 \text{ eV}$.

This gives a rate of emission of alk^+ from grains of size a^i (termed ion emission) of

$$\mathcal{R}_{\text{alk}^+ \text{ evap}}^i = f_+^i n_{\text{alk cond}}^i \nu_{\text{evap}} = \nu_{\text{alk}^+}^i n_{\text{alk cond}}^i. \quad (11)$$

Therefore, the rate of emission of neutral atoms (alk^0) from grains of size a^i is

$$\mathcal{R}_{\text{alk}^0 \text{ evap}}^i = (1 - f_+^i) n_{\text{alk cond}}^i \nu_{\text{evap}} = \nu_{\text{alk}^0}^i n_{\text{alk cond}}^i. \quad (12)$$

The ability of grains to convert alk^0 to alk^+ through ion emission is an important contributor to the ionization fraction of the disc at high temperatures (Desch & Turner 2015).

As Desch & Turner (2015) also noted, at high temperatures grains are able to emit electrons from their surface due to thermionic emission. For grains of size a^i and charge Z^i , electrons are emitted at a rate

$$\mathcal{R}_{\text{therm}}^i(Z^i) = n_{\text{gr}}^i 4\pi (a^i)^2 \lambda_R \frac{4\pi m_e (kT)^2}{h^3} \exp\left(-\frac{W_{\text{eff}}^i}{kT}\right), \quad (13)$$

where λ_R is the Richardson constant, experimentally $\approx 1/2$ (Crowell

1965). We take its value to be exactly 1/2 in our calculations. At high temperatures, equation 13 shows that the grains will also positively contribute to the ionization state through emission of electrons.

2.3 Reaction network

The above processes give rise to the following equilibrium reaction network (where starred equations will be invoked further below)

$$\begin{aligned} \frac{dn_{\text{gr}}^i Z^i}{dt} &= \mathcal{R}_{\text{alk}^+, \text{ads}}^i(Z^i) + \mathcal{R}_{\text{m}^+, \text{ads}}^i(Z^i) + \mathcal{R}_{\text{M}^+, \text{ads}}^i(Z^i) - \mathcal{R}_{\text{e}, \text{ads}}^i(Z^i) \\ &+ \mathcal{R}_{\text{therm}}^i(Z^i) - \mathcal{R}_{\text{alk}^+ \text{ evap}}^i(Z^i) = 0 \end{aligned} \quad (14^*)$$

$$\begin{aligned} \frac{dn_{\text{alk}^+}}{dt} &= -\mathcal{R}_{\text{gas}, 3\text{-rec}, \text{alk}^+} - \mathcal{R}_{\text{gas}, 2\text{-rec}, \text{alk}^+} + \mathcal{R}_{\text{gas}, \text{coll-ion}} \\ &+ \sum_i \mathcal{R}_{\text{alk}^+ \text{ evap}}^i(Z^i) - \sum_i \mathcal{R}_{\text{alk}^+, \text{ads}}^i(Z^i) = 0 \end{aligned} \quad (15^*)$$

$$\begin{aligned} \frac{dn_{\text{e}}}{dt} &= +\zeta n_{\text{H}_2} - \mathcal{R}_{\text{gas}, 2\text{-rec}, \text{M}^+} - \sum_i \mathcal{R}_{\text{e}, \text{ads}}^i(Z^i) - \mathcal{R}_{\text{diss-rec}} \\ &- \mathcal{R}_{\text{gas}, 2\text{-rec}, \text{alk}^+} - \mathcal{R}_{\text{gas}, 3\text{-rec}, \text{alk}^+} + \mathcal{R}_{\text{gas}, \text{coll-ion}} \\ &+ \sum_i \mathcal{R}_{\text{therm}}^i(Z^i) = 0 \end{aligned} \quad (16^*)$$

$$\frac{dn_{\text{m}^+}}{dt} = +\zeta n_{\text{H}_2} - \mathcal{R}_{\text{ct}} - \mathcal{R}_{\text{diss-rec}} - \sum_i \mathcal{R}_{\text{m}^+, \text{ads}}^i(Z^i) = 0 \quad (17^*)$$

$$\frac{dn_{\text{M}^+}}{dt} = +\mathcal{R}_{\text{ct}} - \mathcal{R}_{\text{gas}, 2\text{-rec}, \text{M}^+} - \sum_i \mathcal{R}_{\text{M}^+, \text{ads}}^i(Z^i) = 0 \quad (18)$$

$$\begin{aligned} \frac{dn_{\text{alk}^0}}{dt} &= \mathcal{R}_{\text{gas}, 2\text{-rec}, \text{alk}^+} + \mathcal{R}_{\text{gas}, 3\text{-rec}, \text{alk}^+} - \mathcal{R}_{\text{gas}, \text{coll-ion}} \\ &+ \sum_i \mathcal{R}_{\text{alk}^0 \text{ evap}}^i(Z^i) - \sum_i \mathcal{R}_{\text{alk}^0, \text{ads}}^i(Z^i) = 0 \end{aligned} \quad (19)$$

$$\frac{dn_{\text{alk cond}}^i}{dt} = \mathcal{R}_{\text{alk}^+, \text{ads}}^i(Z^i) + \mathcal{R}_{\text{alk}^0, \text{ads}}^i(Z^i) - \mathcal{R}_{\text{alk evap}}^i = 0, \quad (20)$$

where all rates dependent on grain charge are explicitly indicated with a suffix (Z^i). In addition to the above equations, we have an equation for charge conservation

$$\sum_i Z^i n_{\text{gr}}^i + n_{\text{alk}^+} + n_{\text{m}^+} + n_{\text{M}^+} - n_{\text{e}} = 0. \quad (21)$$

Equation (20) is linear in $n_{\text{alk cond}}^i$ and provides the equilibrium value of $n_{\text{alk cond}}^i$ directly

$$n_{\text{alk cond}}^i = \frac{1}{\nu_{\text{evap}}} (\nu_{\text{alk}^+}^i n_{\text{alk}^+} + \nu_{\text{alk}^0}^i n_{\text{alk}^0}). \quad (22)$$

In combination with $n_{\text{alk tot}} = n_{\text{alk}^+} + n_{\text{alk}^0} + \sum_i n_{\text{alk cond}}^i$, this provides the equilibrium value of n_{alk^0} in terms of n_{alk^+}

$$n_{\text{alk}^0} = \frac{n_{\text{alk tot}} - \left(1 + \frac{\sum_i \nu_{\text{alk}^+}^i}{\nu_{\text{evap}}}\right) n_{\text{alk}^+}}{1 + \frac{\sum_i \nu_{\text{alk}^0}^i}{\nu_{\text{evap}}}}. \quad (23)$$

Therefore, we solve the subset of equations (14*) – (17*) for $[Z^1, \dots, Z^{N_{\text{gr}}}, n_{\text{alk}^+}, n_{\text{e}}, n_{\text{m}^+}]$, with n_{m^+} given by the charge conservation equation.

$$n_{\text{M}^+} = n_{\text{e}} - \sum_i Z^i n_{\text{gr}}^i - n_{\text{alk}^+} - n_{\text{m}^+} \quad (24)$$

2.3.1 Solution techniques

We have used two techniques to solve the above system of equations: (1) a globally convergent, relatively slow non-linear successive over-relaxation (nSOR) method (see e.g., [Ortega & Rheinboldt 2000](#)); and (2) a locally convergent, faster multidimensional Newton-like method. The first method is employed for finding initial guesses, while the second is employed for evolutionary calculations where parameter values, e.g. T , P , f_{dg} , are changed by small amounts. We can also evolve between two sets of significantly differing parameter values by incrementally evolving the parameters with the Newton-like method to prevent divergence from the root while maintaining speed.

Our system of equations can be represented as $\mathbf{F}(E_1, \dots, E_N) : \mathbb{R}^N \rightarrow \mathbb{R}^N$, where the equations E_i correspond to equations (14*) – (17*) and N (as throughout) is the number of equations (i.e., $N = N_{\text{gr}} + 3$). Each of these equations depends on the set of parameters, $x_i : i \in [1, N]$, i.e., on the values \mathbf{Z} for each grain size in the distribution, n_{alk^+} , n_e , n_{m^+} .

The i th step of the k th iteration of the nSOR method works by finding the root of the i th equation with respect to x_i . The root of this equation is denoted \hat{x}_i .

$$E_i(x_1^{(k)}, \dots, x_{i-1}^{(k)}, \hat{x}_i, \dots, x_N^{(k-1)}) = 0 \quad . \quad (25)$$

Note that the variables $x_j : j \in [1, i-1]$ take the value assigned to them at the k th iteration, while the variables $x_j : j \in [i+1, N]$ take their values from those at the $k-1$ th iteration.

The variable x_i is updated at the k th iteration to

$$x_i^{(k)} = x_i^{(k-1)} + \omega^{(k)} (\hat{x}_i - x_i^{(k-1)}) \quad , \quad (26)$$

where $\omega^{(k)}$ is the relaxation parameter for the k th iteration with value in range (0, 2). For a fixed relaxation parameter of unity, successive over-relaxation is equivalent to the Gauss–Seidel method. The term over-relaxation reflects the possibility of having $\omega^{(k)}$ exceed unity. Typically the first few iterations require a value of $\omega^{(k)}$ which is less than unity, while later iterations can be allowed to approach the solution faster by a choice of $\omega^{(k)}$ in range (1, 2). Of order 100–1000 iterations are typically required to achieve an initial guess that enables the Newton-like method to converge.

The Newton-like method chosen is the modified Powell’s Hybrid method ([Powell 1970](#)) first implemented in MINPACK ([Moré et al. 1984](#)) and subsequently in GSL ([Galassi et al. 2009](#)). We use the latter in this work. This is a trust-region algorithm, which first computes the Newton step $\delta \mathbf{x}_N$ by inverting $\mathbf{J} \delta \mathbf{x}_N = -\mathbf{F}$ (where \mathbf{J} is the Jacobian matrix of the vector \mathbf{F}). The components of the Jacobian matrix are computed analytically. If the step is within the trust-region $|\delta \mathbf{x}| < \delta$ (the default value $\delta = 100$), it is accepted. Otherwise, the step taken is a linear combination of the Newton step $\delta \mathbf{x}_N = -\mathbf{J}^{-1} \mathbf{F}$ and the gradient direction of $|\mathbf{F}|^2$.

$$\delta \mathbf{x} = -\alpha \mathbf{J}^{-1} \mathbf{F} - \beta \nabla |\mathbf{F}|^2 \quad , \quad (27)$$

where α and β are constants chosen to minimize $|\mathbf{F}|^2$, while keeping $\delta \mathbf{x}$ within the trust-region. We set a criterion of $|\mathbf{F}| < 10^{-7}$ for convergence. Of order 10 iterations are typically required to achieve convergence.

2.4 Validity of chemical equilibrium

To assume chemical equilibrium in the context of a protoplanetary disc, the chemical time-scale must be shorter than the dynamical

time-scale, thermal time-scale, and the shortest time-scale for collisions between grains. The first two conditions ensure constant n_{H_2} and T , and also ensure that dynamics do not change the dust distribution. The third condition ensures that the underlying grain size distribution does not evolve collisionally on the time-scales of chemical reactions and that charge exchange between grains is negligible. Note that, if viscous heating provides the dominant heating rate (as we expect in the inner disc), the thermal time-scale ($\sim t_{\text{dyn}}/\alpha$) is (much) longer than the dynamical time-scale t_{dyn} (since $\alpha < 1$). Therefore, the thermal time-scale does not further constrain the chemical time-scale and is omitted from the analysis. Below, we show how we calculate the chemical and grain collision time-scales.

2.4.1 Chemical time-scale

To determine the chemical time-scale, we consider the time-scales for small perturbations away from the equilibrium solution to decay. The full system, equations (14*) – (20), without assuming equilibrium may be written in vector form

$$\dot{\mathbf{x}} = \mathbf{F}(\mathbf{x}) \quad . \quad (28)$$

Away from equilibrium, we have two constraints: charge conservation (equation 21); and the constraint that alk number densities (n_{alk^0} , n_{alk^+} , $n_{\text{alk cond}}^i$) must sum to $n_{\text{alk}}^{\text{tot}}$. To avoid linear dependence due to these constraints, we remove equations (18) and (19) from the system.

The system may be linearized about equilibrium i.e. $\mathbf{x} = \mathbf{x}_0 + \Delta \mathbf{x}$, $\dot{\Delta \mathbf{x}} = \mathbf{J} \Delta \mathbf{x}$ to give

$$\dot{\Delta \mathbf{x}} = \mathbf{F}(\mathbf{x}_0 + \Delta \mathbf{x}) \approx \mathbf{F}(\mathbf{x}_0) + \mathbf{J}(\mathbf{x}_0) \Delta \mathbf{x} \quad , \quad (29)$$

where \mathbf{J} is the Jacobian matrix.

Considering a perturbation about equilibrium of the form $\Delta \mathbf{x} \propto e^{\lambda t}$, an eigen equation must be solved for the values of λ

$$(\mathbf{J} - \lambda \mathbf{I}) \Delta \mathbf{x} = \mathbf{0} \quad . \quad (30)$$

For a stable equilibrium, it is required that the real part of λ_i satisfies $\Re(\lambda_i) < 0 \forall i$. Provided this is satisfied, the chemical time-scale will be

$$t_{\text{chem}} = \max \left(\frac{1}{|\Re(\lambda_i)|} \right) \quad . \quad (31)$$

Concurrently, the dynamical time-scale, at semi-major axis r , is

$$t_{\text{dyn}}(r) = \frac{1}{\Omega_K(r)} \quad , \quad (32)$$

where $\Omega_K(r)$ is the Keplerian frequency at r .

2.4.2 Grain collision time-scale

The shortest time-scale for one grain to collide with another is given by

$$t_{\text{coll. dust}} = \min_{i,j} \left(\frac{1}{K_{ij} n_{\text{gr}}^j} \right) \quad , \quad (33)$$

where K_{ij} is termed the collision kernel. The full collision kernel is defined in [Okuzumi et al. \(2011a\)](#) as an integral over the Maxwellian distribution of relative velocities $\Delta \mathbf{v}_{ij}$, centred on $\Delta \mathbf{v}_{ij}^D$, the sum of the systematic (non-Brownian) relative velocity sources (or drift velocities). This distribution may be denoted as $P(|\Delta \mathbf{v}_{ij} - \Delta \mathbf{v}_{ij}^D|)$. Hence, we have

$$K_{ij} = \int P(|\Delta \mathbf{v}_{ij} - \Delta \mathbf{v}_{ij}^D|) \sigma_{ij} |\Delta \mathbf{v}_{ij}| d\Delta \mathbf{v}_{ij} \quad , \quad (34)$$

where σ_{ij} is the collision cross-section including the *Coulomb* electrostatic interaction between the grains. Note that the velocities are defined at infinite separation.⁵

Okuzumi et al. (2011a) provide limiting forms for K_{ij} (now referring to absolute values of the velocities without the vector notation) in the case of like charged particles interacting through a Coulomb potential:

$$K_{ij} \approx \begin{cases} \pi(a_i + a_j)^2 \times \\ \Delta v_{ij}^{\text{Br}} \exp\left(-\frac{U(a_i + a_j)}{kT}\right), & \text{if } \Delta v_{ij}^D \ll \Delta v_{ij}^{\text{Br}}, \end{cases} \quad (35a)$$

$$\begin{cases} \pi(a_i + a_j)^2 \times \\ \Delta v_{ij}^D \left(1 - \frac{U(a_i + a_j)}{\text{KE}_{ij}^D}\right), & \text{if } \Delta v_{ij}^D \gg \Delta v_{ij}^{\text{Br}}. \end{cases} \quad (35b)$$

where $U(a_i + a_j)$ is the electrostatic potential at the point of contact, $\Delta v_{ij}^{\text{Br}} = \left(\frac{8kT(m_i + m_j)}{\pi m_i m_j}\right)^{\frac{1}{2}}$ is the relative velocity due to Brownian

motion and $\text{KE}_{ij}^D = \frac{1}{2} \frac{m_i m_j}{m_i + m_j} (\Delta v_{ij}^D)^2$ is the kinetic energy due to drift at infinite separation. Note that, formally equation (35b) is only applicable in the limit $\text{KE}_{ij}^D \gg U(a_i + a_j)$, i.e., weak Coulomb effects. However, we, like Akimkin et al. (2023), use this limiting form for the entire range $\text{KE}_{ij}^D > U(a_i + a_j)$, for the purpose of computational efficiency. Also following Akimkin et al. (2023), we set $K_{ij} = 0$, if $\text{KE}_{ij}^D < U(a_i + a_j)$. In reality, a non-zero K_{ij} persists, because there will always be a contribution to K_{ij} due to the Maxwellian distribution of velocities, even when $\Delta v_{ij}^D \gg \Delta v_{ij}^{\text{Br}}$.

Akimkin et al. (2023) also derive a form for σ_{ij} including the effect of a dipole between the grains, which requires root-finding for each pairwise interaction; for computational efficiency we avoid this complication.

Sources of (non-Brownian) relative velocities Δv_{ij}^D between grains include: turbulent eddies (Ormel & Cuzzi 2007), settling (Weidenschilling 1980), radial and azimuthal drift (Weidenschilling 1977) and ambipolar drift (Guillet et al. 2020). We consider each of these in turn.

Turbulence

We take the relative velocities due to turbulence $\Delta v_{ij}^{\text{turb}}$ to be given by the limiting solutions provided in equations (26), (28) and (29) of Ormel & Cuzzi (2007).

Settling

Differential settling of dust grains gives a contribution

$$\Delta v_{ij}^{\text{settle}} = |\Delta \text{St}_{ij}| \Omega_K z, \quad (36)$$

where z is the vertical displacement above the mid-plane and $|\Delta \text{St}_{ij}|$ is the absolute value of the difference in the dimensionless stopping

⁵ The screening-length (e.g. Debye length), due to the re-distribution of electrons surrounding each charged grain, is shorter than the mean free path of grains for all but the highest densities, temperatures and dust-to-gas ratios, and lowest ionization fractions. In this region of parameter space, the changing relative velocity of grains Δv_{ij} (due to the electrostatics), as they approach one another, will affect the collision rate appreciably. Considering this effect makes Δv_{ij}^D a function of the impact parameter b and separation of the grains r . Therefore, K_{ij} should be computed as an integral over b and r . We leave this complication to later work, if required.

times (Stokes numbers) of particles i and j . To determine the Stokes number, we must know which drag regime we are in: Stokes ($a \gtrsim l_{\text{mfp}}$, where a is the particle size and l_{mfp} is the mean free path of gas) or Epstein ($a \lesssim l_{\text{mfp}}$). In terms of the disc variables, the mean free path of gas is:

$$l_{\text{mfp}} = \frac{1}{n\sigma} \approx 5 \left(\frac{n_{\text{H}_2}}{10^{14} \text{ cm}^{-3}} \right)^{-1} \text{ cm}, \quad (37)$$

where n is the gas number density, and $\sigma \approx 2 \times 10^{-15} \text{ cm}^{-2}$ is the cross-section for collisions between gas particles, assumed to be H_2 molecules. The approximate mean-free path we have derived exceeds the maximum grain size $a_{\text{max}} = 0.1 \text{ cm}$ that we use; therefore, we expect to be within the Epstein regime at 1 au.

In the Epstein regime, the dimensionless stopping time of a particle is

$$\text{St}_i = \frac{\rho_{\text{gr}} a^i}{\rho_c s} \Omega_K. \quad (38)$$

If we are not in the Epstein regime, either due to the presence of large particles or an increase in density (at smaller semi-major axis), we merely have to compute a form of the dimensionless stopping time valid for the Stokes regime.

Radial and azimuthal drift

The terms due to radial and azimuthal drift depend on the underlying disc structure; therefore, their inclusion is left to future work where a disc model is present. However, in the inner disc, where the dimensionless stopping times are small, we expect these contributions to be small.

Ambipolar drift

The final driver of relative velocities that we consider is ambipolar drift (Guillet et al. 2020). In the context of protoplanetary discs, while polycyclic aromatic hydrocarbons (PAHs) may be well-coupled to the field (Mohanty et al. 2013), grains are not; therefore, the relative velocity due to ambipolar drift is negligible. To see this, consider the Hall parameter for grains, β_{gr} (ratio of the gyrofrequency of grains to their collision frequency with neutrals, which measures the degree to which grains are coupled to the field).

$$\beta_{\text{gr}} = \frac{|Z|eB}{m_{\text{gr}}c} \frac{1}{\gamma_{\text{gr}}\rho_n} \approx 6 \times 10^{-6} |Z| \left(\frac{B}{10 \text{ G}} \right) \left(\frac{a}{10^{-5} \text{ cm}} \right)^{-2} \times \left(\frac{T}{800 \text{ K}} \right)^{-\frac{1}{2}} \left(\frac{n_{\text{H}_2}}{10^{14} \text{ cm}^{-3}} \right)^{-1}, \quad (39)$$

where $\gamma_{\text{gr}} = \langle \sigma v \rangle_{\text{gr}} / (m_{\text{gr}} + m_n) \approx \langle \sigma v \rangle_{\text{gr}} / m_{\text{gr}}$ is the drag coefficient for the grains due to collisions with the neutrals, $\langle \sigma v \rangle_{\text{gr}}$ being the rate constant for momentum transfer between grains and neutrals, m_{gr} is the mass of a given grain and m_n the mass of the neutrals. The density of the neutrals is $\rho_n \approx \mu m_{\text{H}} n_{\text{H}_2}$. We follow Mohanty et al.

(2013) in using $\langle \sigma v \rangle_{\text{gr}} = \pi a^2 \left(\frac{128kT}{9\pi m_n} \right)^{\frac{1}{2}} \text{ cm}^3 \text{ s}^{-1}$, from Wardle & Ng (1999). Note that β_{gr} is independent of the mass of the grain m_{gr} , and depends only on the grain cross-sectional area a^2 .

We see from equation (39) that $\beta_{\text{gr}} \ll 1$, and thus the grains are completely decoupled. From the weak dependence of β_{gr} on disc properties, we do not expect this to change throughout the inner disc. Therefore, relative velocity due to ambipolar drift may be neglected.

Combining sources

Relative velocities between grains are typically combined in quadrature (e.g., [Robinson et al. 2024](#))

$$\Delta v_{ij}^D = \sqrt{|\Delta \mathbf{v}_{ij}^{\text{lam}}|^2 + (\Delta v_{ij}^{\text{turb}})^2}, \quad (40)$$

where $\Delta \mathbf{v}_{ij}^{\text{lam}}$ is the drift velocity between two grains due to laminar sources, while $\Delta v_{ij}^{\text{turb}}$ is the drift velocity due to turbulence. Note that we have not included a source due to Brownian motion in the above equation, as this is already accounted for by the integration over a Maxwellian in equation (34). Of the sources that we have listed, the only laminar source of relative velocities that we consider is due to settling.

In this work, we shall compute the time-scales for collisions between grains due to Brownian motion, turbulence and settling separately. For Brownian motion, we use the first limiting solution in equation (34) to compute $t_{\text{coll. dust}}^{\text{Br}}$. For turbulence and settling, we use the second limiting solution of equation (34). Instead of summing velocities in quadrature, i.e. equation (40), $\Delta v_{ij}^D = \Delta v_{ij}^{\text{turb}}$ is used to compute $t_{\text{coll. dust}}^{\text{turb}}$ and $\Delta v_{ij}^D = \Delta v_{ij}^{\text{settle}}$ used to compute $t_{\text{coll. dust}}^{\text{settle}}$. If $t_{\text{coll. dust}}^{\text{turb}}$ or $t_{\text{coll. dust}}^{\text{settle}}$ is the shortest time-scale, the overall shortest time-scale for collisions between grains $t_{\text{coll. dust}}$ can then be, at most, a factor of $\sqrt{2}$ shorter (if $t_{\text{coll. dust}}^{\text{turb}} = t_{\text{coll. dust}}^{\text{settle}}$). Otherwise if $t_{\text{coll. dust}}^{\text{Br}}$ is shorter than the other dust collision time-scales $t_{\text{coll. dust}} = t_{\text{coll. dust}}^{\text{Br}}$.

3 RESULTS

3.1 Tests

3.1.1 Desch & Turner (2015)

Here we: (i) verify that the results of our network, with a distribution of grain sizes, agree with those of the single grain size network of [Desch & Turner \(2015\)](#), in the limit of the distribution of grain sizes tending to a single size; and (ii) investigate the change in the ionization state caused by broadening the grain size distribution.

To test that our network is consistent with that of [Desch & Turner \(2015\)](#), we first simplify the physics of our network to more closely match theirs. Specifically, we remove the intermediate molecular ion species m^+ from our network and assume a 100% efficiency of charge transfer from H_2^+ to M^0 . This entails replacing the charge transfer term in equation (18) with ζn_{H_2} , and removing the dissociative recombination term from equation (16*).

With this simplified physics in our network, we compute the ionization fractions in the disc as a function of a_{max} . For comparison with [Desch & Turner \(2015\)](#), we use the same disc parameters they do: an MRN distribution with $q = 3.5$ and $a_{\text{min}} = 10^{-4}$ cm, dust-to-gas ratio $f_{\text{dg}} = 0.01$, $T = 1000$ K and $n_{\text{H}_2} = 10^{14}$ cm $^{-3}$. The value of $a_{\text{min}} = 10^{-4}$ cm (which is different from our fiducial value of 10^{-5} cm) is chosen to match the single grain size used by [Desch & Turner \(2015\)](#). We have also used $\zeta = 1.4 \times 10^{-22}$ s $^{-1}$, established by [Jankovic et al. \(2021\)](#) to be the actual non-thermal ionization rate that [Desch & Turner \(2015\)](#) had used in their simulations.

With the physics and parameter values matching those used by [Desch & Turner \(2015\)](#), our results are plotted in Fig. 1. It is clear that our network converges to the single grain size network of [Desch & Turner \(2015\)](#) in the limit that our distribution collapses to a single grain size i.e., as $a_{\text{max}} \rightarrow a_{\text{min}}$.

Conversely, as a_{max} increases, i.e., as the distribution broadens,

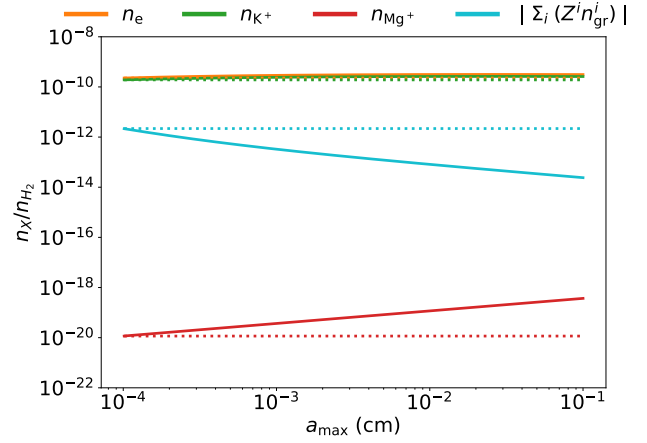


Figure 1. Solid lines show number densities of charged species as a function of the maximum grain size of the distribution of grains, a_{max} with $a_{\text{min}} = 10^{-4}$ cm, $q = 3.5$ and $f_{\text{dg}} = 0.01$. $|\Sigma_i (Z^i n_{\text{gr}}^i)|$ shows the total charge density on the grains. The temperature $T = 1000$ K and $n_{\text{H}_2} = 10^{14}$ cm $^{-3}$. The dotted line shows the [Desch & Turner \(2015\)](#) result for a single grain size with $a = a_{\text{min}}$. As expected, the abundances for the network with a distribution of grains tends to this [Desch & Turner \(2015\)](#) result as $a_{\text{max}} \rightarrow a_{\text{min}}$.

our network moves away from the single grain size results. As a_{max} increases at fixed dust-to-gas ratio (i.e., fixed total mass of grains), the total surface area of grains decreases.

First, as a_{max} increases, the decreased total surface area causes a decrease in the total amount of charge condensed on the grains. Second, the Mg^+ abundance increases with increased a_{max} , also due to the reduced total surface area for adsorption of Mg^+ . Third, the electrons and K^+ behave differently from Mg^+ . Mg^+ is produced exclusively in the gas-phase, but this is not true for electrons and K^+ . As we shall see, the dominant mechanism for production of electrons and K^+ are on the surface of the grains. On the one hand, this means that, as we decrease the total surface area, we decrease the rate of K^0 adsorption, which is required to produce electrons and K^+ on the grains. On the other hand, there is a proportionate decrease in the rate of adsorption of electrons and K^+ with decreased total surface area of grains. Taken together, this means that the abundance of electrons and K^+ stay approximately constant as a function of a_{max} .

3.1.2 Marchand et al. (2022)

[Marchand et al. \(2022\)](#) solve an equilibrium chemical network with: (i) a slightly different solution technique to our own; and (ii) a distribution of charges for each grain size. We wish to verify that our network and solution technique can reproduce their results. To do this, we must first align our physics with [Marchand et al. \(2022\)](#). This includes excluding: thermionic and ion emission; the molecular ion, intermediate between H_2^+ and the metal ion (Mg^+). Conversely, we include non-thermal ionization of the alkali metal (which has little practical impact, and is thus not included elsewhere). We incorporate these choices in our network. On the other hand, we ignore charge transfer between the metal (Mg) and alkali (K) (which is a small effect), but do include three-body gas recombination for the alkali ions, in our calculation of their network.

The parameters we choose are an MRN distribution of dust grains with $q = 3.5$ with $a_{\text{min}} = 10^{-5}$ cm, $a_{\text{max}} = 10^{-1}$ cm, $f_{\text{dg}} = 0.01$ and $n_{\text{H}_2} = 10^{14}$ cm $^{-3}$.

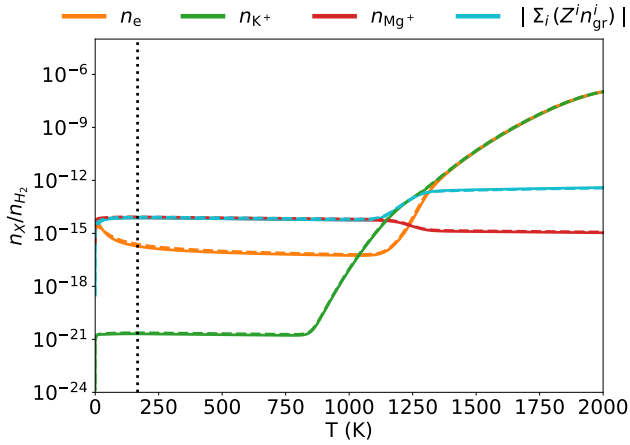


Figure 2. Ionization as a function of T of our network (solid) and the Marchand et al. (2022) network (dashed) with modifications described in the text for $q = 3.5$ and $a_{\min} = 10^{-5}$ cm, $a_{\max} = 10^{-1}$ cm, $f_{\text{dg}} = 0.01$ and $n_{\text{H}_2} = 10^{14}$ cm $^{-3}$. $|\Sigma_i(Z^i n_{\text{gr}}^i)|$ shows the total charge density on the grains. The black dashed vertical line indicates the temperature above which $\tau \equiv akT/e^2 > 1$ for all grains in the network (see 3.3 for the significance of $\tau > 1$). Good agreement between the models is obtained for all T , not simply those temperatures where $\tau > 1$ for all grains.

The comparison is shown in Fig. 2. We see an excellent agreement between the two models, despite the difference in solution technique and absence of a distribution of grain charges for each grain size in our model. We discuss the reason for the last point in Subsection 3.3.

3.1.3 Result of tests

We have seen that our network reproduces the abundances obtained previously for a single grain size, and the abundances obtained with a similar network for a distribution of grain sizes but without ion and thermionic emission.

3.2 Network behaviour

In this section, we seek to isolate the impact of grains in our network and explore this impact as a function of temperature.

In Fig. 3, we plot the equilibrium number densities of species as a function of temperature: *solid lines* show the case of our full network including grains (i.e., solving the full network described in Subsection 2.3), while *dashed lines* show the no-grain case (i.e., excluding the grain terms from our network). Both cases are for a single value of $n_{\text{H}_2} = 10^{14}$ cm $^{-3}$. We discuss the behaviour in the low and high temperature regimes below.

3.2.1 Low temperature

At low temperatures ($T \lesssim 500$ K for the dusty case, $T \lesssim 1100$ K for the dust-free case), we see that the dominant charged species in the gas-phase are electrons and Mg^+ , our metal ion. This is a result of non-thermal ionization, producing electrons and molecular ions (here these are HCO^+ ions). These molecular ions then transfer their charge to neutral metal atoms (here Mg^0), making Mg^+ .

In the model with grains, we see that the abundances of electrons and Mg^+ are orders of magnitude lower than in the dust-free case,

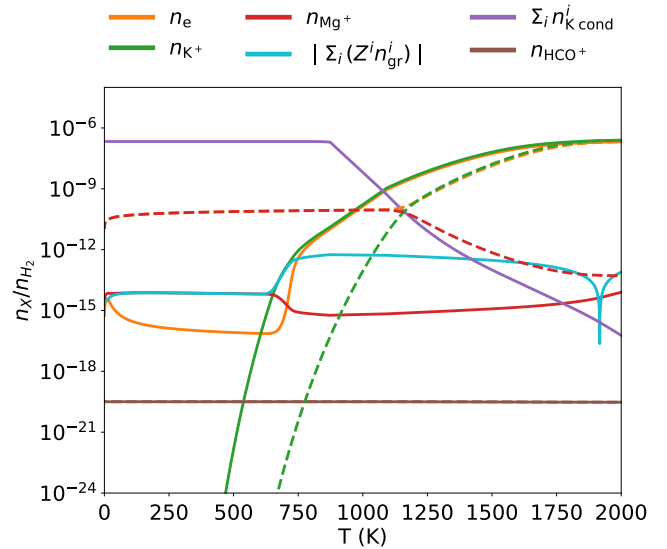


Figure 3. Solid lines show number densities as a function of temperature for an MRN distribution of grains with $a_{\min} = 10^{-5}$ cm, $a_{\max} = 10^{-1}$ cm, $q = 3.5$ and $f_{\text{dg}} = 0.01$. Dashed lines show the grain-free case (for which there is no condensed potassium or grain charge). For the case with grains, $|\Sigma_i(Z^i n_{\text{gr}}^i)|$ shows the total charge density on the grains and $|\Sigma_i(n_{\text{K}^i \text{cond}}^i)|$ is the total number density of condensed potassium on the grains. For both cases, $n_{\text{H}_2} = 10^{14}$ cm $^{-3}$.

implying that adsorption onto grains is the dominant mechanism for removing these species from the gas-phase.

Moreover, in the model with grains, at temperatures $\lesssim 600$ K, we see that the electron abundance decreases with increasing temperature. This is due to the increased thermal velocity of the electrons: as the velocity increases with temperature, electrons can overcome the electrostatic repulsion of the negatively charged grains, and are thus adsorbed onto the grains. Note that Mg^+ is actually attracted to negatively charged grains; there is no repulsion to overcome, and its gas phase abundance remains approximately constant below $\lesssim 600$ K. Once the electrons cross the electrostatic repulsion barrier of the grains, their abundance in the gas-phase become orders of magnitudes below the abundance of Mg^+ on account of their larger thermal velocities.

Finally, in both the dusty and dust-free cases, and throughout the temperature range, the abundance of the molecular ion (HCO^+) is identical and constant. This implies that the HCO^+ abundance is not dependent on the other gas phase abundances. This can only be the case if charge transfer is the dominant pathway for removal of HCO^+ . In this case, the HCO^+ abundance depends only on the number density of neutral metal atoms n_{Mg^0} that charge is transferred to, and $n_{\text{Mg}^0} \approx n_{\text{Mg}^{\text{tot}}} = \text{constant}$ due to the large total abundance of Mg .

3.2.2 High temperature

For both the network with grains and without, a sharp increase in the ionized potassium abundance as a function of temperature is observed due to thermal ionization sources. For the network with grains, this rise begins at lower temperature. This is due to ion emission from the grain surface. If the grains are not too negatively charged, the work function of the grains is a deeper potential well than the ionization

potential of the alkali atom. This means all the neutral alkali on the grain surface lose their outermost electron to the grains. When evaporation of these K^+ from the surface of the grains begins to occur at sufficiently high temperatures ($kT \rightarrow E_a$), the gas phase number density of K^+ increases rapidly. Since the activation energy of the grains (E_a) is lower than the first ionization potential of potassium (for $kT \rightarrow IP$ collisional ionization of potassium occurs in the gas phase), ion emission is able to increase the abundance of potassium ions in the gas phase considerably at a lower temperature than is possible without grains.

After the increase in the potassium ion abundance with T , for the model with grains, there is a small lag before the electron abundance also increases with temperature. As the gas phase potassium ion abundance increases with temperature due to ion emission, the grains become more negatively charged. Coupled with the increased thermal energy, this means electrons can more readily escape the grains through thermionic emission. The origin of the lag in temperature for this to occur is the fact that the grain charge must become more negative, and the thermal energy greater, until the effective work function of the grains can be overcome. As noted by [Desch & Turner \(2015\)](#), this is when $|Ze^2/a| \rightarrow W$. When the temperature becomes sufficiently high, both the K^+ ion and electron produced by ionization of K^0 on the surface of the grains are immediately released. Thermionic emission becomes increasingly efficient; hence, the grains become more positive.

The average charge on grains as a function of temperature is plotted in Fig. 4, and compared to the average grain charge we would obtain without ionic and thermionic emission. At low temperatures ($T \lesssim 600$ K), the average grain charge for the networks with and without emission is identical, since no emission process is important at these temperatures. Above this threshold, the average grain charge in the network with emission decreases rapidly to a minimum. This sharp change in average grain charge with temperature, in the network with emission, is due to the exponential onset of ion emission once $kT \rightarrow E_a$. At the minimum of the grain charge, ionization of K^0 to K^+ on the surface of the grains is impeded, and recombination of K^+ on the surface becomes more favourable. Emission of electrons through thermionic emission also increases with increasing temperature. Both of these factors conspire to increase the average grain charge with increasing temperature.

On the other hand, the average charge for the network without emission remains roughly constant until the temperature exceeds ~ 1200 K. Above this temperature, the average grain charge decreases, rapidly at first due to the onset of collisional ionization, and then more slowly as electrons gain higher thermal velocities.

Note that we use silicate grains in our network, which should sublimate at ≥ 1500 K. However, at these temperatures the abundance of gas-phase species converge to the same values for the dusty and grain-free cases, so correcting for the sublimation of grains would not alter the gas phase abundances significantly.

3.3 Distribution of charge on grains

In this section, we discuss the grain charge as a function of grain size and temperature. We first illustrate our results using our fiducial MRN distribution (but, as we show in Subsection 3.5 and in Appendix C, the shape of the distribution is immaterial).

To facilitate this discussion, it is useful to define a ‘‘reduced temperature’’: $\tau(a, T) \equiv akT/e^2$. In their seminal work, [Draine & Sutin \(1987\)](#) found a linear relationship between the average grain charge on a grain of given size, and the grain size for $\tau \geq 1$, a result which is widely used (e.g., [Okuzumi 2009](#); [Marchand et al. 2021](#)). However,

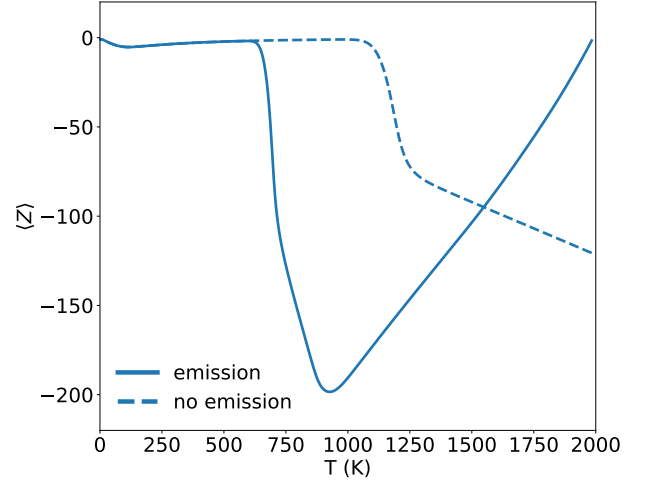


Figure 4. The solid line shows the average charge on the grains, $\langle Z \rangle = \sum_i Z^i n_{gr}^i / \sum_i n_{gr}^i$, as a function of temperature for an MRN distribution of grains with $a_{\min} = 10^{-5}$ cm, $a_{\max} = 10^{-1}$ cm, $q = 3.5$ and $f_{dg} = 0.01$ at $n_{H_2} = 10^{14}$ cm $^{-3}$. The dashed line illustrates the case for the same population of grains and n_{H_2} , but without the inclusion of thermionic or ion emission.

they did not include ionic and thermionic emission. We wish to test if a similar result still holds when these emissions are included (though we do not include a distribution of charges for a given grain size).

Fig. 5 shows the grain charge as a function of grain size for $T = [10 \text{ K}, 100 \text{ K}, 1000 \text{ K}]$. It is immediately apparent that a linear relationship with a common slope is present in the log–log plots for all values of the temperature, at least for larger grain sizes. The grain size beyond which this relationship emerges is around the grain size for which $\tau = 1$. This grain size decreases with increasing temperature.

The slope of this linear relationship in the log–log plot is unity, thus $Z \propto a$. Therefore, $Z \propto a$ not only for low temperature, in the limit where ion emission and thermionic emission are negligible, but also at high temperature, where both of these processes are active. The reason for the above is discussed in Appendix C.

If the straight line in the log–log plot were extrapolated, the intercept of this extrapolated straight line determines the constant of proportionality between Z and a . It is clearly a function of T . We term this constant of proportionality ψ ; this is the same notation used by [Draine & Sutin \(1987\)](#).

We also note that the magnitude of the charge on the grains increases with increasing temperature; this is the result of the combined gas and grain-phase processes.

3.4 Effect of grain size distribution

Here we examine the effect of changing the input grain size distribution, keeping dust-to-gas ratio constant. The distributions used are MRN, with: the fiducial $q = 3.5$; a distribution more strongly peaked at smaller grains, $q = 5.0$; and a distribution which is flatter as a function of grain size, $q = 2.0$.

The fiducial $q = 3.5$ has its mass dominated by large grains but its surface area dominated by small grains. The steeper value of $q = 5$ has both its surface area and mass dominated by small grains, giving a significantly larger total surface area for a given dust-to-gas ratio. Conversely, the $q = 2$ distribution has both its mass and surface area

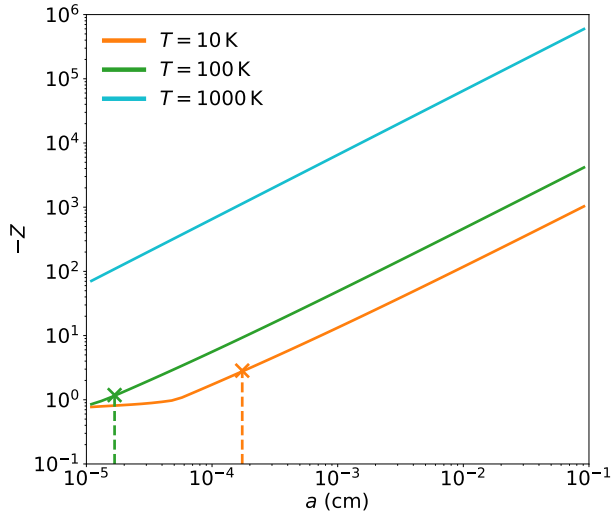


Figure 5. Grain charge as a function of binned grain size (50 bins) in an MRN population of dust grains with $a_{\min} = 10^{-5}$ cm, $a_{\max} = 10^{-1}$ cm, $q = 3.5$ and $f_{\text{dg}} = 0.01$. The grain size within the distribution for which $\tau = 1$ for each temperature is depicted with a vertical dashed line and a cross. At $T = 1000$ K, all grains within the distribution have $\tau \gtrsim 1$. We see that the linear relationship for $\tau \gtrsim 1$ is observed for all temperatures.

dominated by large grains. This leads to a significantly smaller total surface area.

Increased total surface area of the grains has been shown to reduce gas-phase abundances of charged species in the absence of ion and thermionic emission (Bai & Goodman 2009); we wish to explore how different grain size distributions affect the abundances with these effects included.

In Fig. 6, the ionization fractions as a function of temperature obtained with $q = 5$ and shallower $q = 2$ are separately compared to the fiducial value of $q = 3.5$. As expected, the $q = 5$ distribution, with the largest total surface area, has significantly lower number densities of gas phase species at low temperature. The $q = 2$ distribution, having the smallest total surface area, has significantly higher gas phase number densities. Lower total surface areas correspond to more negative values of ψ at low temperature. A more negative ψ implies a more negative charge on a given grain size bin.

Ion emission produces a steep rise in the potassium number density at $T \gtrsim 500$ K, regardless of the grain size distribution. This is because, what limits ion emission at these temperatures is evaporation from the grains, i.e., not the process of producing potassium ions from potassium atoms on the surface of the grains. The evaporation temperature is evidently independent of the grain size distribution used; therefore, so is the threshold temperature for appreciable ion emission.

Lower total surface area (in this comparison, lower q), means that ion emission produces a more negative value of ψ for a given temperature, since each grain becomes more negatively charged. Since thermionic emission requires sufficiently negative ψ , distributions with lower ψ achieve an appreciable increase in the electron number density due to thermionic emission at lower T . This sequence is shown in Fig. 7.

Total surface area may also be altered by changing the total dust-to-gas ratio (i.e., total grain mass for a fixed gas mass). For example,

thermionic emission would begin at a lower temperature if the grain surface area were decreased by decreasing the dust-to-gas ratio.

We note that this trade-off between total grain surface area and the dust-to-gas ratio has been employed in previous work, to approximate the effects of a grain size-distribution with a single grain size and an “effective dust-to-gas ratio” (Jankovic et al. 2021; Bai & Goodman 2009). As we show in Appendix D, this method mostly yields reliable number densities for the dominant gas-phase charged species (and is thus useful for calculating fluid resistivities). However, as we also show in Appendix D, this technique predicts a total grain charge that can (in some regions of parameter space) diverge by an order of magnitude or more compared to the true value explicitly calculated in this paper. Moreover, since it considers only a single grain size by definition, this technique cannot capture the grain charge as a function of grain size, unlike the explicit method here (see Subsection 3.3 for our grain charge distribution results). For both reasons, when considering phenomena that are directly and explicitly affected by the grain charge (e.g., most importantly, coagulation/fragmentation calculations), the “effective dust-to-gas ratio” method is inadequate, and the full explicit calculation shown in this paper is required.

3.5 An arbitrary grain size distribution

Grain size distributions, resulting from fragmentation-coagulation and dynamics, are typically more complex than a simple MRN distribution. To integrate this network self-consistently within codes that include this dust physics, our network must be able to take arbitrary distributions as inputs. We show that we may compute the chemical abundances for such arbitrary distributions.

We have constructed a fictitious distribution which has the logarithm of the number density of grains log-normally distributed with respect to the grain size about a mean of 10^{-4} cm, with a standard deviation σ of 1 decade, i.e. $\log_{10} n(a) = Ae^{-(\log_{10}(a) - (-4))^2/2}$. We have cut off this distribution below $-\sigma$ and above $+\sigma$, to match the values of $a_{\min} = 10^{-5}$ cm and $a_{\max} = 10^{-1}$ cm that we have used elsewhere in this work. The normalization A was fixed so that the dust-to-gas ratio at $n_{\text{H}_2} = 10^{14}$ cm $^{-3}$ with $\mu = 2.34$ is 0.01. This distribution is plotted in Fig. 8.

We plot the abundances as a function of temperature, with $n_{\text{H}_2} = 10^{14}$ cm $^{-3}$, for this distribution of grains in Fig. 9 and, to provide some physical intuition, compare to the abundance we get from a network with a single size of 10^{-4} cm (the peak of our fictitious distribution) and the same dust-to-gas ratio of 0.01.

Below 1000 K, when potassium is largely condensed on the grains, the gas-phase abundances of the distribution of grains are significantly larger. Due to the mass of the distribution of grains being dominated by the larger grains, the total surface area of grains for fixed dust-to-gas ratio is lower than for the network with a single grain size of 10^{-4} cm.

Beyond 1000 K, as in Fig. 6, the potassium and electron abundances of the distribution and single size networks converge. However, grain charge and Mg $^+$ abundances is significantly different in both cases.

In Fig. 10, we show the grain charge as a function of grain size for the arbitrary distribution. We plot this for the same values of $T = [10 \text{ K}, 100 \text{ K}, 1000 \text{ K}]$ that we chose for the MRN distribution whose grain charge as a function of grain size we plotted in Fig. 5. This illustrates that the linear relationship between grain charge and grain size at fixed temperature is not dependent on the distribution being a power law.

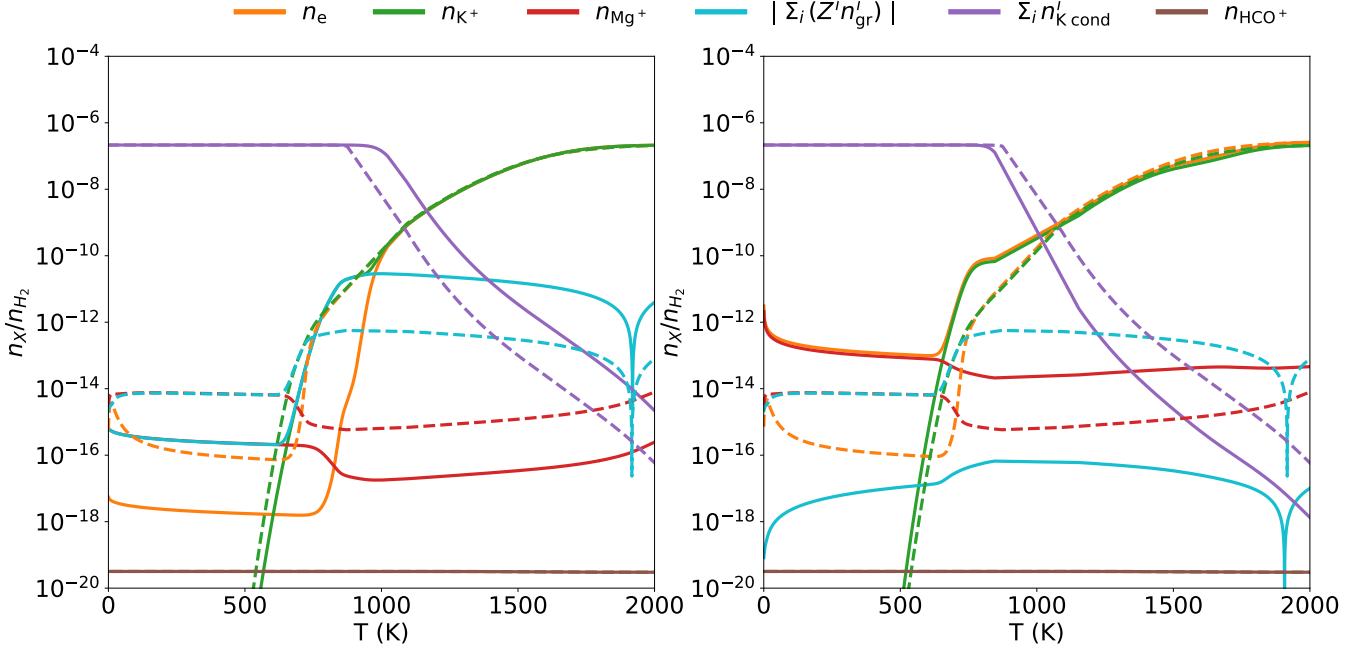


Figure 6. The ionization fractions of the reaction network are shown for MRN distributions with $q = 5$ (left, solid) and $q = 2$ (right, solid) and compared with the ionization state produced by an MRN distribution with the fiducial $q = 3.5$ slope (left and right, dashed). The remaining parameters used are the fiducial $a_{\min} = 10^{-5}$ cm, $a_{\max} = 10^{-1}$ cm and $f_{\text{dg}} = 0.01$ for fixed $n_{\text{H}_2} = 10^{14}$ cm $^{-3}$. $|\Sigma_i(Z^i n_{\text{gr}}^i)|$ shows the total charge density on the grains and $|\Sigma_i(n_{\text{K}^i}^{\text{cond}})|$ is the total number density of condensed potassium on the grains.

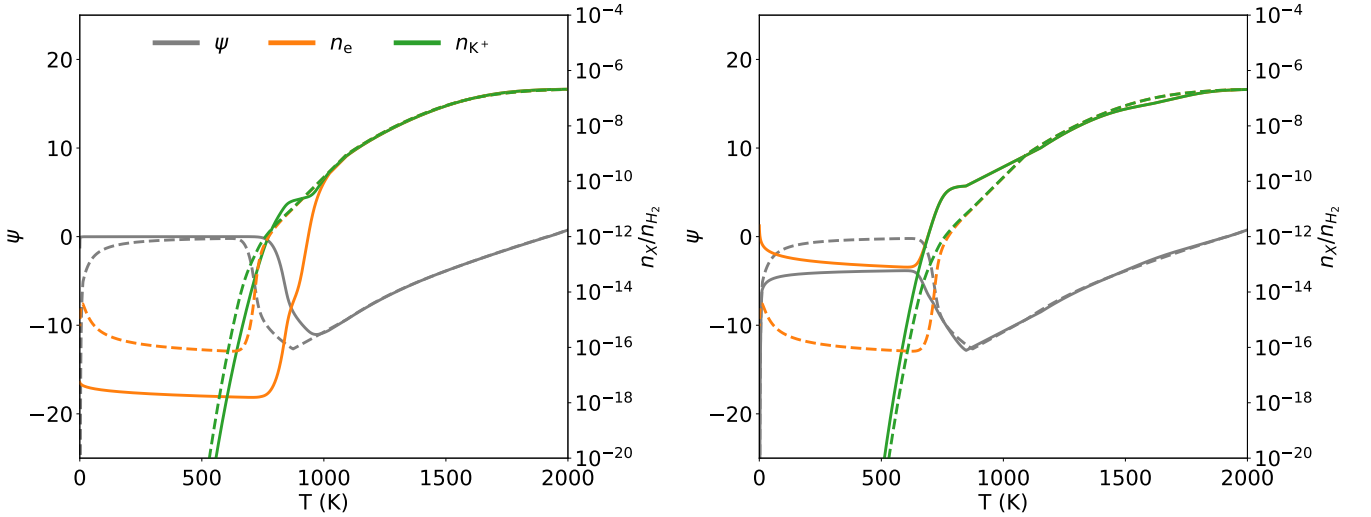


Figure 7. $\psi (= Z/\tau)$, number densities of electrons (n_e) and potassium ions (n_{K^+}) as a function of temperature, T , for the same MRN distributions as in Fig. 6 i.e. $q = 5$ (left, solid) and $q = 2$ (right, solid) compared to the fiducial $q = 3.5$ (dashed). As in the models in Fig. 6, the remaining parameters are the fiducial $a_{\min} = 10^{-5}$ cm, $a_{\max} = 10^{-1}$ cm with $n_{\text{H}_2} = 10^{14}$ cm $^{-3}$.

3.6 Validity of chemical equilibrium

Following the method in 2.4, we compute the relevant time-scales (i.e., equations (31) – (33)) for our network as a function of temperature for conditions applicable to the disc mid-plane at 1 au ($n_{\text{H}_2} = 10^{14}$ cm $^{-3}$) and two scale heights above our mid-plane value at 1 au ($n_{\text{H}_2} = 10^{14} \exp(-2)$ cm $^{-3}$). We also compute the time-scale associated with each species within our network. The time-scale for

species x is defined as $t_x = x/\mathcal{R}_{\pm x}$, where $\mathcal{R}_{\pm x}$ is either the sum of all rates of production or the sum of all rates of destruction of species x ; either of these choices are equivalent in equilibrium. Furthermore, we compute the chemical time-scale that we would obtain if potassium were omitted altogether $t_{\text{chem, no K}}$.

We show these chemical time-scales as a function of temperature for mid-plane conditions at 1 au in Fig. 11. We have shaded regions not relevant for our study in grey, these are: (i) where the chemical

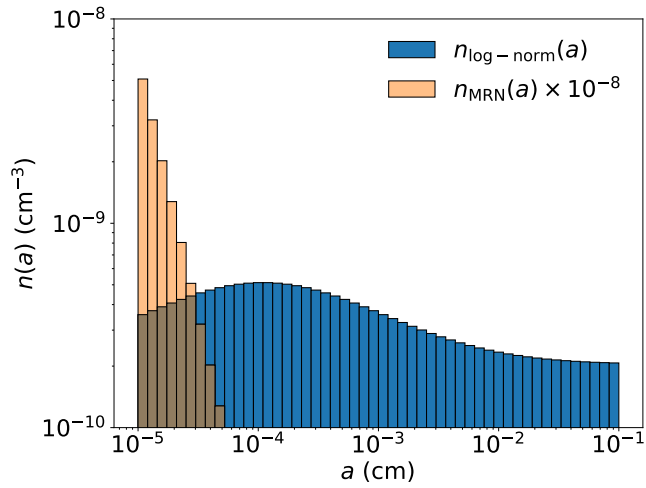


Figure 8. The blue histogram shows the number densities in each grain size bin of a fictitious dust distribution with the logarithm of the number density of grains log-normally distributed about a mean of 10^{-4} cm, with a standard deviation σ of 1 decade. The distribution has been cut off below -1σ and above $+3\sigma$, and normalized to produce a dust-to-gas ratio of 0.01 at $n_{\text{H}_2} = 10^{14} \text{ cm}^{-3}$. For comparison, overplotted in orange is 10^{-8} times the number density of grains for an MRN distribution with the fiducial parameters $a_{\text{min}} = 10^{-5}$ cm, $a_{\text{max}} = 10^{-1}$ cm, $q = 3.5$ and $f_{\text{dg}} = 0.01$ at the same density of $n_{\text{H}_2} = 10^{14} \text{ cm}^{-3}$.

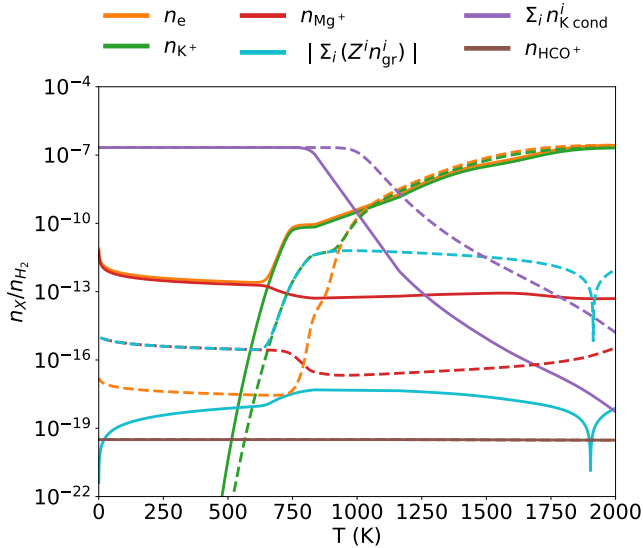


Figure 9. Abundances as a function of temperature T , for the fictitious distribution (solid) shown in Fig. 8, and grains with a single size of 10^{-4} cm (dashed). Both networks have $n_{\text{H}_2} = 10^{14} \text{ cm}^{-3}$ and $f_{\text{dg}} = 0.01$. $|\Sigma_i (Z^i n_{\text{gr}}^i)|$ shows the total charge density on the grains and $\Sigma_i (n_{\text{K}^i_{\text{cond}}})$ is the total number density of condensed potassium on the grains.

time-scale is shorter than the dynamical time-scale (incidentally, this threshold produces a minimum temperature $T \sim 800$ K, similar to that which we expect for the mid-plane at 1 au (Jankovic et al. 2021)); and $T \gtrsim 1500$ K, greater than the sublimation temperature of silicate grains.

We see that the chemical time-scale t_{chem} of the whole system

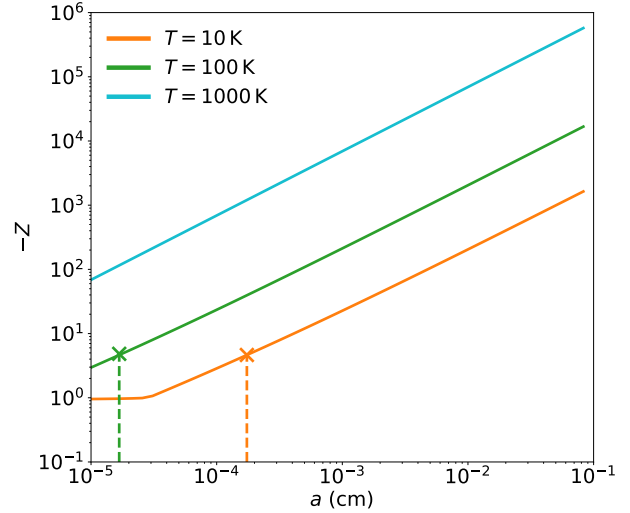


Figure 10. The same plot of grain charge as a function of binned grain size (50 bins) as in Fig. 5, except for the fictitious distribution shown in Fig. 8 with $f_{\text{dg}} = 0.01$ at $n_{\text{H}_2} = 10^{14} \text{ cm}^{-3}$ and $\mu = 2.34$. The grain size within the distribution for which $\tau = 1$ for each temperature is depicted with a vertical dashed line and a cross. At $T = 1000$ K, all grains within the distribution have $\tau \gtrsim 1$. We see that the linear relationship for $\tau \gtrsim 1$ is observed for all temperatures.

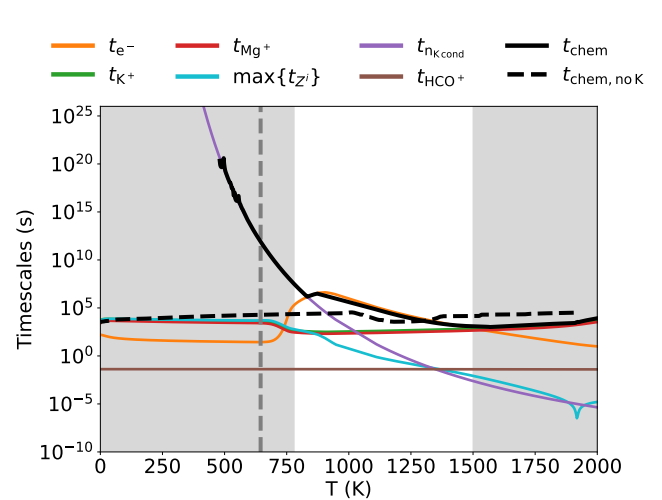


Figure 11. Comparison of chemical time-scales for $n_{\text{H}_2} = 10^{14} \text{ cm}^{-3}$. The relevant chemical time-scale is t_{chem} (the full system) to the right of the vertical dashed line, and $t_{\text{chem, no K}}$ (the system excluding potassium) to its left. The other time-scales plotted are the time-scales associated with individual species t_x . The longest of these individual time-scales maps on to the chemical time-scale t_{chem} .

follows the longest of any of the individual species time-scales t_x . At the largest temperatures, the longest time-scales for any individual species are those associated with Mg^+ and K^+ . Since these species are produced through non-thermal and thermal ionization respectively, but have similar time-scales, the limiting time-scale must be due to a common destruction rate. This destruction rate corresponds to adsorption onto grains, which is indeed the largest

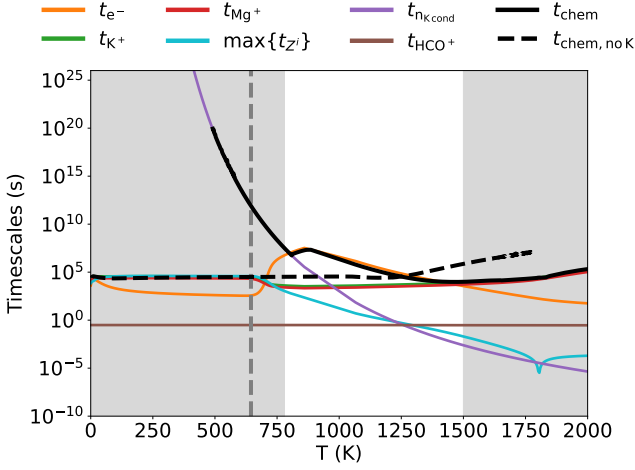


Figure 12. The same plot as Fig. 11, but for $n_{\text{H}_2} = 10^{14} \exp(-2) \text{ cm}^{-3}$, equivalent to two scale heights above the mid-plane value at approximately 1 au. Very similar behaviour is observed.

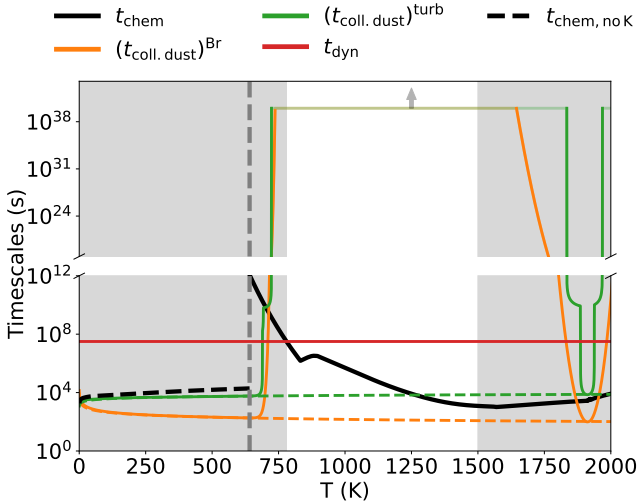


Figure 13. Comparison of time-scales for $n_{\text{H}_2} = 10^{14} \text{ cm}^{-3}$. The relevant chemical time-scale is t_{chem} (the full system) to the right of the vertical dashed line, and $t_{\text{chem, no K}}$ (the system excluding potassium) to its left. Dust collision time-scales for Brownian motion and turbulence are shown with the effect of grain charge included (solid) and excluded (dashed). Where grain charge is included, the grain collision time-scales in the region of interest (unshaded) become many orders of magnitude greater than all other system time-scales. In these regions, the chemical time-scale is also shorter than the other relevant time-scales, indicating that chemical equilibrium is valid. (Note that our grain collision time-scales, with charge included, reach a plotted plateau of 10^{40} s, shown in a lighter colour. In reality, the time-scales are even higher in this region, as indicated by the upward arrow. We have simply truncated our calculations here.)

rate of destruction for both these species at these temperatures. For $900 \text{ K} \lesssim T \lesssim 1500 \text{ K}$, the electron time-scale is the longest. In this region, it is the rate of thermionic emission which is the dominant mechanism for production of electrons, while the dominant method of destruction is due to collisions with the negatively charged grains. Below 900 K , non-thermal ionization is the dominant production

mechanism for electrons, while collisions with grains remains the dominant destruction mechanism.

However, the limiting time-scale for the system as a whole below 900 K is not due to the electrons, but the condensed potassium. The evaporation time-scale becomes exponentially longer with decreasing temperature. At small enough temperatures, this sends the maximum $\mathfrak{R}(\lambda_i)$, found by solving equation (29), towards zero; eventually its value oscillates between positive (indicating an unstable equilibrium) and negative values. We clip the chemical time-scale where this occurs as this oscillation is purely due to finite numerical precision. If we consider a network without potassium, the chemical time-scale does not increase exponentially as $T \rightarrow 0 \text{ K}$ as seen in Fig. 11. As T decreases from 900 K , the thermal ionization rates becomes smaller than the non-thermal ionization rate, and the abundances of all species other than potassium are identical in the case with potassium or without. Here, for the purposes of determining the resistivities or grain charges, the inclusion of potassium is of no consequence. The temperature below which potassium does not appreciably alter the abundances of other species is shown with a vertical dashed line in Fig. 11. Hence, the chemical time-scale of interest is that of this reduced system with no potassium, shown in the black dashed line in Fig. 11. This time-scale is considerably reduced compared to the full system time-scale and matches the time-scales associated with potassium ions, magnesium ions and grains in the full system. This implies that the limiting time-scale is due to collisions of ions with grains.

The complementary plot, corresponding to two scale heights above this mid-plane density is shown in Fig. 12. Similar behaviour can be seen. However, time-scales are typically somewhat longer due to the lower densities.

We now compare the chemical time-scale to the other system time-scales, namely the dynamical time-scale and the dust collision time-scales. This is plotted for a density applicable to the mid-plane at 1 au ($n_{\text{H}_2} = 10^{14} \text{ cm}^{-3}$) in Fig. 13. For mid-plane conditions, the chemical time-scale, with the inclusion of the effect of charge on the dust collision rates, is shorter than all other system time-scales throughout the majority of the temperature range plotted (and throughout the whole unshaded range in which we are interested). This is with the exception of two regions: (i) close to 2000 K , where the grain charge transitions through zero (negative at low temperature to positive at high temperature due to the effect of thermionic emission); and (ii) $\lesssim 750 \text{ K}$, where the chemical time-scale increases due to the rapidly decreasing rate of evaporation of potassium from the grains with decreasing temperature. Furthermore, below 750 K the grain collision time-scales decrease with decreasing temperature as the grains are less negatively charged (see Fig. 4). At temperatures leftwards of the vertical dashed line, the chemical time-scale with no potassium becomes the chemical time-scale of interest. In this region, this chemical time-scale is shorter than the dynamical time-scale but still longer or comparable to the dust collision time-scales. Nevertheless, these regions are not germane for the reasons stated above.

In sum, since the chemical time-scale is the shortest of all time-scales in a temperature range and density applicable to the mid-plane at 1 au (e.g., Jankovic et al. 2021), chemical equilibrium is a good approximation here.

Apart from in the regions near 2000 K and $\lesssim 750 \text{ K}$, the grain–grain collision time-scales are so long, due to the negative charge on the grains, that a size distribution may be ‘frozen in’ after entering the inner disc.

This paints a rosier picture for the survival of large grains in the inner disc than that presented by Akimkin et al. (2023). Their

charging model, which does not account for thermionic and ion emission, produces lower magnitude grain charges.

This lower charging means that only a subset of all grain collisions are forbidden by the electrostatic barrier in their model. These are collisions between smaller grains. Small grains may still undergo collisions in their model, but must collide with larger grains. Since these collisions occur with relatively large relative velocity in their calculations for higher turbulence (as found in the inner disc (Mohanty et al. 2018; Jankovic et al. 2021)), a collision with a grown grain will typically occur with an impact velocity greater than the fragmentation velocity (for a fragmentation velocity of 1 m s^{-1}).

This means that their grain size distribution evolves towards a distribution very sharply peaked at the smallest grain sizes (see their Fig. 4 showing the evolving distribution for typical inner disc parameters).

In our model of the charging, all collisions between grains at the mid-plane are orders of magnitude longer than the dynamical time, indicating that the distribution does not evolve collisionally. If grains can become large outside the inner disc, this grain charging can conserve their sizes. This difference has profound implications for the opacity and thus the disc structure.

The time-scales of our network, two-scale heights above the value we adopt for the mid-plane at 1 au, are shown in Fig. 14. Due to the lower density of the gas, the chemical time-scale becomes longer but remains below the dynamical time-scale in the region of interest. This implies that chemical equilibrium is expected to be a good approximation throughout the vertical extent of the disc near the inner edge of the dead-zone. The shortest dust collision time-scale is now due to settling, which in some temperature ranges may become shorter than the chemical time-scale. Nevertheless, this is far above the mid-plane; the dust-to-gas ratio should be lower here than the value used in this calculation $f_{dg} = 0.01$ due to the effect of dust settling. This means that collisions between grains should be more infrequent than indicated here. We conclude that chemical equilibrium is also a good approximation here.

3.7 Resistivities

Obtaining resistivities for non-ideal MHD calculations, that incorporate the effect of a distribution of grains, with the inclusion of ion and thermionic emission, is one of the primary motivations for this work. As such, we provide illustrative calculations of these resistivities below. The resistivities are computed following the method of Wardle (2007). We have assumed a constant r.m.s magnetic field B of 10 G, informed by the values computed by Jankovic et al. (2021).

In Fig. 15, we show the Ohmic, Hall and ambipolar resistivities as a function of temperature, at the fiducial density ($n_{\text{H}_2} = 10^{14} \text{ cm}^{-3}$). The grain distributions used are MRN, with: the fiducial $q = 3.5$, the more sharply peaked $q = 5.0$ and flatter $q = 2.0$. We use the fiducial minimum and maximum grain size $a_{\text{min}} = 10^{-5} \text{ cm}$ and $a_{\text{max}} = 10^{-1} \text{ cm}$ with $f_{dg} = 10^{-2}$.

In both panels, we see that all resistivities are low in the high temperature limit due to relatively high ionization fractions. When electrons are the dominant negative charge carriers (throughout the entire temperature range for $q = 2.0$, see Fig. 6), they are the best coupled species to the field, and the Hall resistivity is positive. At lower temperatures, the grains become the dominant negative charge carriers (for $q = 3.5$ and $q = 5.0$, see Fig. 6). Since the grains are more decoupled from the field than the ions, the Hall current changes direction relative to the case where electrons are the dominant negative charge carriers. This means that the Hall resistivity becomes negative. The magnitude of the Hall current is also weakened when

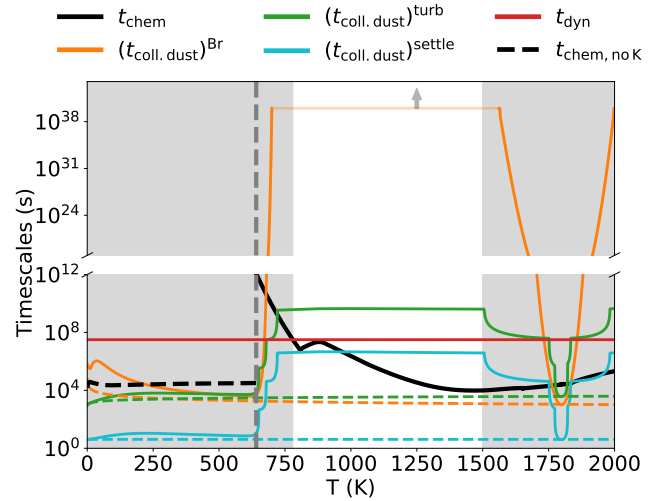


Figure 14. Comparison of time-scales for $n_{\text{H}_2} = 10^{14}/e^2 \text{ cm}^{-3}$, applicable to two scale-heights above the mid-plane value of the number density used in Fig. 13. The time-scale for collisions between grains due to settling is now considered and found to be the shortest of the grain–grain collision time-scales. (Note that our grain collision time-scales, with charge included, reach a plotted plateau of 10^{40} s , shown in a lighter colour. In reality, the time-scales are even higher in this region, as indicated by the upward arrow. We have simply truncated our calculations here.)

the electrons become sub-dominant negative charge carriers, and the magnitude of the Hall resistivity decreases.

This transition from electrons being dominant negative charge carriers to grains also causes a decrease in the ambipolar diffusion, as the grains have a much weaker coupling to the field. Further decreases in temperature produce larger magnitude resistivities, which ultimately saturate as the dominant ionization fractions plateau (because the ionization is non-thermal, and temperature independent, and the recombination rate depends only weakly on temperature).

4 CONCLUSIONS

In this paper, (1) we investigate a chemical network that applies to the inner regions of protoplanetary discs. The network includes electrons, molecular hydrogen, an alkali species, a non-alkali metal, a molecular ion, and grains with an arbitrary size distribution. We consider non-thermal ionization of hydrogen (by, e.g., XUV irradiation, cosmic rays and radioactivity), thermal ionization of alkalis, charge transfer between gas-phase species, gas–grain chemistry, ionic and thermionic emission from grain surfaces, and grain charging. (2) We present a numerical technique to solve this network *exactly* (to numerical precision), in equilibrium. The solution technique may, without loss of generality, be extended to multiple alkali, metal, and molecular species (as we demonstrate with two alkali species). (3) We also provide a general method to estimate the chemical time-scale for a network, and (4) supply analytic expressions for grain–grain collision time-scales for charged grains.

We validate our equilibrium results against earlier work, in relevant limits. We further discuss the physical reasons for our results when all the above effects are included, in various parameter regimes.

An important result of this work is that the grain charge is directly proportional to the grain size, above a minimum grain size. This result has previously been shown to hold in the absence of ionic and

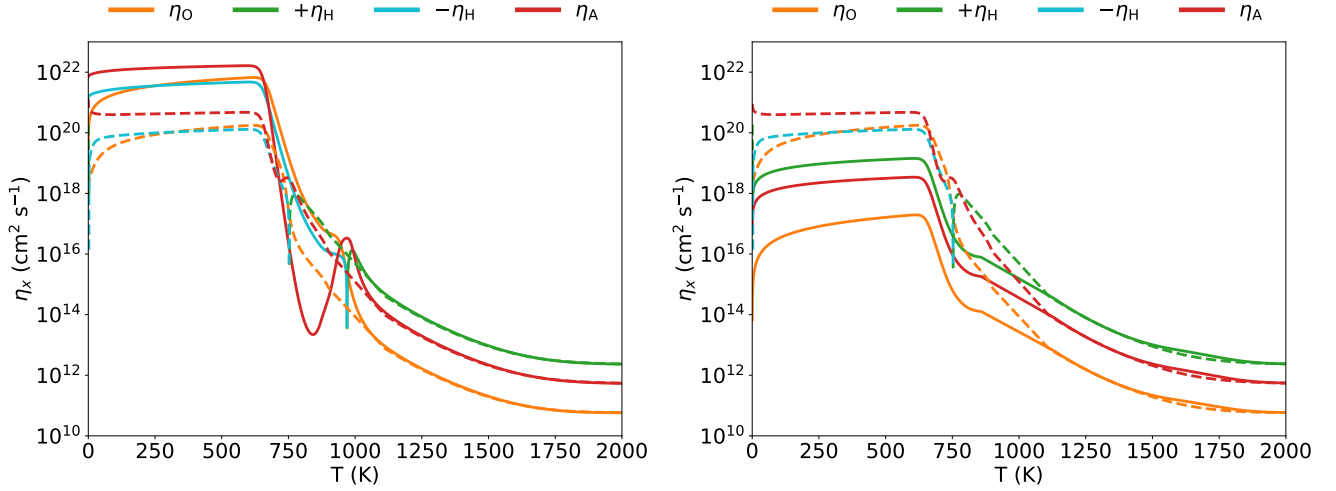


Figure 15. The Ohmic (η_O), Hall (η_H) and ambipolar (η_A) resistivities computed using ionization fractions computed by our reaction network for MRN distributions with $q = 5$ (left, solid) and $q = 2$ (right, solid) compared with the fiducial $q = 3.5$ slope (left and right, dashed). The remaining parameters used are the fiducial $a_{\min} = 10^{-5}$ cm, $a_{\max} = 10^{-1}$ cm and $f_{dg} = 0.01$ for fixed $n_{H_2} = 10^{14}$ cm $^{-3}$ and $B = 10$ G.

thermionic emission; we show here that it continues to hold when these effects are included, and explicate the reason for this behaviour in Appendix C.

We further show that approximating the effect of a range of grain charges via the “effective dust-to-gas-ratio” method, as done in earlier work, yields significantly erroneous grain charges. Finally, we show that grain charging has a very significant effect on grain collision time-scales (and grain collision velocities).

While we have shown, for illustrative purposes, results at 1 au for a fiducial disc density, our network and results are valid throughout the “inner disc” regions, where thermal ionization of alkali species is efficient. As such, our chemical network, and the techniques provided for analysing it, are valuable for calculating the fluid resistivities, and thus the fluid viscosity, in the inner disc (as calculated in, e.g., Mohanty et al. 2018; Jankovic et al. 2021). Moreover, our grain charging results – both the amount of charging as a function of grain size, and the effect of grain charging on grain collision time-scales and velocities – are vital for discerning the fragmentation / coagulation outcomes of grain collisions, and thus for grain and disc evolution under inner disc conditions.

ACKNOWLEDGEMENTS

MW acknowledges the support of a Science and Technologies Facilities Council (STFC) PhD studentship. MW and SM thank James Owen, Marija Jankovic, Neal Turner for extremely helpful discussions that helped sharpen the analysis of this paper. We also thank the anonymous referee for their careful reading and detailed comments, which were highly useful in improving the paper.

DATA AVAILABILITY

The data underlying this article will be shared on reasonable request to the corresponding author.

REFERENCES

- Akimkin V. V., Ivlev A. V., Caselli P., 2020, *ApJ*, **889**, 64
 Akimkin V., Ivlev A. V., Caselli P., Gong M., Silsbee K., 2023, *ApJ*, **953**, 72
 Ashton A., Hayhurst A., 1973, *Combustion and Flame*, **21**, 69
 Asplund M., Grevesse N., Sauval A. J., Scott P., 2009, *ARA&A*, **47**, 481
 Bai X.-N., 2011, *ApJ*, **739**, 50
 Bai X.-N., Goodman J., 2009, *ApJ*, **701**, 737
 Bai X.-N., Stone J. M., 2011, *ApJ*, **736**, 144
 Balbus S. A., Hawley J. F., 1991, *ApJ*, **376**, 214
 Balduin T., Woitke P., Jørgensen U. G., Thi W. F., Narita Y., 2023, *A&A*, **678**, A192
 Blandford R. D., Payne D. G., 1982, *MNRAS*, **199**, 883
 Crowell C. R., 1965, *Solid State Electronics*, **8**, 395
 Desch S. J., Turner N. J., 2015, *ApJ*, **811**, 156
 Draine B. T., 2016, *ApJ*, **831**, 109
 Draine B. T., Sutin B., 1987, *ApJ*, **320**, 803
 Dzyurkevich N., Turner N. J., Henning T., Kley W., 2013, *ApJ*, **765**, 114
 Fleming T. P., Stone J. M., Hawley J. F., 2000, *ApJ*, **530**, 464
 Fujii Y. I., Okuzumi S., Inutsuka S.-i., 2011, *ApJ*, **743**, 53
 Galassi M., Davies J., Theiler J., Gough B., Jungman G., Booth M., Rossi F., 2009, GNU scientific library reference manual. Network Theory Ltd.
 Gammie C. F., 1996, *ApJ*, **457**, 355
 Guillet V., Hennebelle P., Pineau des Forêts G., Marcowith A., Commerçon B., Marchand P., 2020, *A&A*, **643**, A17
 Hagström M., Engvall K., Pettersson J. B. C., 2000, *J. Phys. Chem. B*, **104**, 4457
 Hayashi C., 1981, *Prog. Theor. Phys. Suppl.*, **70**, 35
 Ilgner M., Nelson R. P., 2006, *A&A*, **445**, 205
 Ivlev A. V., Akimkin V. V., Caselli P., 2016, *ApJ*, **833**, 92
 Jankovic M. R., Owen J. E., Mohanty S., Tan J. C., 2021, *MNRAS*, **504**, 280
 Jin L., 1996, *ApJ*, **457**, 798
 Marchand P., Guillet V., Lebreuilly U., Mac Low M. M., 2021, *A&A*, **649**, A50
 Marchand P., Guillet V., Lebreuilly U., Mac Low M. M., 2022, *A&A*, **666**, A27
 Mathis J. S., Rumpl W., Nordsieck K. H., 1977, *ApJ*, **217**, 425
 Millar T. J., Walsh C., Van de Sande M., Markwick A. J., 2024, *A&A*, **682**, A109
 Mohanty S., Ercolano B., Turner N. J., 2013, *ApJ*, **764**, 65
 Mohanty S., Jankovic M. R., Tan J. C., Owen J. E., 2018, *ApJ*, **861**, 144

- Moré J. J., Sorensen D. C., Hillstrom K. E., Garbow B. S., 1984, in Cowell W. R., ed., , Vol. 25, Sources and Development of Mathematical Software. Prentice-Hall, Inc., USA, pp 88–111
- Mori S., Okuzumi S., 2016, *ApJ*, **817**, 52
- Okuzumi S., 2009, *ApJ*, **698**, 1122
- Okuzumi S., Tanaka H., Takeuchi T., Sakagami M.-a., 2011a, *ApJ*, **731**, 95
- Okuzumi S., Tanaka H., Takeuchi T., Sakagami M.-a., 2011b, *ApJ*, **731**, 96
- Oppenheimer M., Dalgarno A., 1974, *ApJ*, **192**, 29
- Ormel C. W., Cuzzi J. N., 2007, *A&A*, **466**, 413
- Ortega J. M., Rheinboldt W. C., 2000, Iterative Solution of Non-linear Equations in Several Variables. SIAM, Philadelphia PA, doi:10.1137/1.9780898719468
- Pneuman G. W., Mitchell T. P., 1965, *Icarus*, **4**, 494
- Powell M. J. D., 1970, in Robinowitz P., ed., , Numerical Methods for Nonlinear Algebraic Equations. Gordon and Breach, London, UK, pp 87–161
- Robinson A., Booth R. A., Owen J. E., 2024, *MNRAS*, **529**, 1524
- Salmeron R., Wardle M., 2008, *MNRAS*, **388**, 1223
- Sano T., Stone J. M., 2002, *ApJ*, **577**, 534
- Sano T., Miyama S. M., Umebayashi T., Nakano T., 2000, *ApJ*, **543**, 486
- Sano T., Inutsuka S.-i., Turner N. J., Stone J. M., 2004, *ApJ*, **605**, 321
- Thi W. F., Lesur G., Woitke P., Kamp I., Rab C., Carmona A., 2019, *A&A*, **632**, A44
- Umebayashi T., Nakano T., 2009, *ApJ*, **690**, 69
- Wardle M., 2007, *Ap&SS*, **311**, 35
- Wardle M., Ng C., 1999, *MNRAS*, **303**, 239
- Weidenschilling S. J., 1977, *MNRAS*, **180**, 57
- Weidenschilling S. J., 1980, *Icarus*, **44**, 172
- Wurm G., Blum J., 1998, *Icarus*, **132**, 125

APPENDIX A: MRI ACTIVITY CRITERIA AND ADOPTED ALKALI

The alkali we include in our chemical network is guided by the desire to achieve a sufficiently high ionization fraction to sustain the MRI. Specifically, efficient MRI in a Keplerian disc requires that the maximum growth rate of MRI-generated local tangled fields, $\sim\Omega$ (the orbital frequency, since the fields are fundamentally amplified by the orbital shear), exceed the Ohmic dissipation rate of the fields, $\sim k^2\eta_O$, where $k \sim \Omega/v_{\mathcal{A}z}$ is the fastest growing vertical mode, $v_{\mathcal{A}z}$ is the vertical component of the local Alfvén velocity, and η_O is the Ohmic resistivity (see [Mohanty et al. 2018](#), and references therein). This results in the Elsasser number criterion for efficient MRI:

$$\Lambda_O \equiv \frac{v_{\mathcal{A}z}^2}{\eta_O\Omega} > 1 \quad . \quad (\text{A1})$$

We derive a simple scaling relation for the Ohmic Elsasser number, Λ_O , as follows. Using the expression for Ohmic resistivity η_O given by [Wardle \(2007\)](#), along with the rate coefficient for collisional momentum transfer between charged species and neutrals from [Wardle & Ng \(1999\)](#), and noting that $\beta_e \gg \beta_i$ (i.e., the Hall parameter for electrons greatly exceeds that for ions), we obtain

$$\eta_O \sim 230 T^{\frac{1}{2}} \mathcal{X}_e^{-1} \quad , \quad (\text{A2})$$

where $\mathcal{X}_e \equiv n_e/n_{\text{H}_2}$ is the ionization fraction, and the $T^{1/2}$ comes from the momentum transfer rate in electron-neutral collisions.

Concurrently, the vertical Alfvén velocity is $v_{\mathcal{A}z} \equiv B_z/\sqrt{4\pi\rho}$, where B_z is the strength of the vertical component of the local field, and ρ is the density. We adopt the results of numerical simulations of the MRI, which indicate that $B_z^2 \sim B^2/25$, where B is the strength of the total local r.m.s. field ([Sano et al. 2004](#)).

We further assume the disc is vertically isothermal (a reasonable approximation for this back-of-the-envelope calculation, at least within a scale-height of the mid-plane in the inner disc; e.g., see

[Jankovic et al. 2021](#)). Then, close to the mid-plane, the density is $\rho \sim \Sigma/z_H$, where Σ is the surface density and $z_H = c_s/\Omega$ is the disc scale-height, for an isothermal sound speed of $c_s = (kT/\mu m_{\text{H}})^{1/2}$ (where μ is the mean molecular weight and m_{H} is the mass of a hydrogen atom). Using $\mu = 2.34$, we obtain

$$v_{\mathcal{A}z}^2 \sim 19 B^2 T^{\frac{1}{2}} \Sigma^{-1} \Omega^{-1} \quad . \quad (\text{A3})$$

Combining equations (A1), (A2) and (A3), the Elsasser number condition finally becomes

$$\Lambda_O \sim 8 \times 10^{-2} \mathcal{X}_e \left(\frac{B^2}{\Sigma\Omega^2} \right) > 1 \quad . \quad (\text{A4})$$

Notice that the explicit dependence on temperature in equations (A2) and (A3) has cancelled out in equation (A4): Λ_O in this formulation only depends on temperature implicitly through whatever T -dependencies \mathcal{X}_e , B and Σ may have.

For a specified set of local disc parameters B , Σ and Ω , equation (A4) yields a threshold value of \mathcal{X}_e that must be exceeded for efficient MRI. Hence, the pertinent alkali(s) to consider will be the one(s) that can surpass this threshold ionization fraction. The local disc parameters will of course depend on the specific disc physics being investigated. As an illustrative example, and to justify the alkali chosen in this paper, we consider: a solar-mass star (implying $\Omega(r) = 2 \times 10^{-7} (r/1 \text{ au})^{-3/2} \text{ s}^{-1}$), surrounded by a disc with a Minimum Mass Solar Nebula (MMSN) surface density profile ($\Sigma(r) = \Sigma_0(r/1 \text{ au})^{-3/2}$; [Hayashi 1981](#)). Equation (A4) then becomes

$$\Lambda_O \sim 10^{11} \mathcal{X}_e \times \left(\frac{\Sigma_0}{1700 \text{ g cm}^{-2}} \right)^{-1} \left(\frac{B}{10 \text{ G}} \right)^2 \left(\frac{r}{1 \text{ au}} \right)^{\frac{9}{2}} > 1 \quad (\text{A5})$$

for the Ohmic Elsasser number around a $1 M_{\odot}$ star, where we have normalized Σ_0 (the surface density at 1 au) by the [Hayashi \(1981\)](#) MMSN value, and the r.m.s. field strength B by the (plausible) value of $\sim 10 \text{ G}$ found by [Jankovic et al. \(2021\)](#) for inner disc regions ($\lesssim 1 \text{ au}$). Equation (A5) says that, in an MMSN-like disc around a solar-mass star, efficient MRI at $\sim 1 \text{ au}$ requires $\mathcal{X}_e > 10^{-11}$ at this location. The radial (r) dependence in equation (A5) also implies that higher ionization fractions are needed closer in (because the Ohmic dissipation rate of the field increases faster than the growth rate with decreasing radius in a vertically isothermal MMSN disc).

To determine which alkali species can produce the requisite ionization fraction \mathcal{X}_e , we first invoke the Saha equation

$$\frac{n_e n_{\text{alk}^+}}{n_{\text{alk}^0}} = \frac{1}{\lambda_e^3} \frac{g_e g_+}{g_0} \exp\left(\frac{-\text{IP}}{kT}\right) \equiv \mathcal{S}(T) \quad , \quad (\text{A6})$$

where $\lambda_e \equiv \sqrt{h^2/(2\pi m_e kT)}$ is the thermal de Broglie wavelength of electrons, and $g_e (= 2)$, $g_0 (= 2)$ and $g_+ (= 1)$ are the degeneracies of the electron, ground state alkali atom and ground state alkali ion respectively. Assuming $n_e \sim n_{\text{alk}^+}$ (i.e., gas-phase ionization of alkalis is the dominant charge-producing process), and $n_{\text{alk}^{\text{tot}}} (\equiv n_{\text{alk}^0} + n_{\text{alk}^+}) \sim n_{\text{alk}^0}$ (weak ionization limit), gives $\mathcal{X}_e \sim \sqrt{\mathcal{S}(T) n_{\text{alk}^{\text{tot}}}/n_{\text{H}_2}^2}$. Using this, we calculate the temperature required for either sodium or potassium (the two most abundant alkalis) to produce the threshold $\mathcal{X}_e \sim 10^{-11}$ needed for MRI at 1 au. Adopting solar photospheric abundances from [Asplund et al. \(2009\)](#) ($x_{\text{H}} = 9.21 \times 10^{-1}$, $x_{\text{Na}} = 1.6 \times 10^{-6}$ and $x_{\text{K}} = 9.87 \times 10^{-8}$, where $x_i \equiv n_i/(\sum_j n_j)$ for any species i), together with the respective alkali ionization potentials ($\text{IP}_{\text{Na}} = 5.14 \text{ eV}$, $\text{IP}_{\text{K}} = 4.34 \text{ eV}$), in the same vertically isothermal MMSN disc invoked above, we infer that sodium reaches the requisite ionization threshold at $T \sim 1180 \text{ K}$, while potassium reaches it at an appreciably lower $T \sim 1060 \text{ K}$ (at this T , sodium is a factor of 20 less

ionized due to its higher IP, in spite of its higher abundance). Thus, *if* gas-phase collisional ionization of alkalis is the primary source of charge, then potassium is the pertinent alkali to consider, at least at ~ 1 au in a vertically isothermal MMSN disc (the fiducial conditions we choose to illustrate our results in this paper.^{6,7})

On the other hand, as we show in this work (and also shown by Desch & Turner 2015), ionic and thermionic emission from grains, following ionization of alkali atoms on grain surfaces, dominate over gas-phase collisional ionization of alkalis as the source of free charges in most of the inner disc. The work function of grains relative to the alkali ionization potential means that, on grain surfaces, ionization of potassium is energetically more favourable than ionization of sodium. Thus, in this case too, potassium is more important than sodium for determining the gas-phase charge abundances (and also for grain charging).

For these reasons, we adopt potassium as the relevant alkali over most of this paper. However, for completeness, we also show the effect of including sodium as an additional alkali, in Appendix B below.

APPENDIX B: INCLUDING ANOTHER ALKALI METAL

Here we consider the impact of adding another alkali to our network. We choose sodium for its large abundance. Relative to potassium, sodium has a lower activation energy of 3.08 eV, a higher first ionization potential of 5.14 eV and a higher abundance of 1.6×10^{-6} (Asplund et al. 2009).

This network is plotted as a function of temperature for our fiducial parameters in Fig. B1. The effect of the reduced activation energy is to produce a larger number density of Na^+ in the gas-phase than that of K^+ below around 600 K. At high enough temperature, the effect of the ionization potential of Na being greater than the ionization potential of K means that the K^+ abundance becomes greater than the Na^+ abundance. At $T \gtrsim 2000$ K, the ionization potential of Na^+ is surmounted and due to the enhanced abundance of Na relative to K, the abundance of Na^+ exceeds the K^+ abundance.

The only parts of the temperature range where the inclusion of Na significantly alters the abundances are around 600 K and above around 2000 K. In these regions, the inclusion of sodium also affects the grain charge. Above 2000 K, this effect is irrelevant as grains should be sublimated. However, the region around 600 K, where Na^+ evaporates from the grain surface will affect the grain charge. Therefore, the effect of Na should ideally be included where fragmentation-coagulation calculations are to be co-evolved with the disc chemistry. However, this is a restricted temperature range and is unlikely to affect things significantly across the disc as a whole.

⁶ More precisely, we have adopted $n_{\text{H}_2} = 10^{14} \text{ cm}^{-3}$ in much of this paper, to facilitate comparison of our results to the existing literature; this corresponds to the mid-plane number density at $T \sim 1000$ K ($\sim T$ at which potassium reaches the threshold \mathcal{X}_e for MRI), in a vertically isothermal MMSN disc at ~ 1 au.

⁷ Gammie (1996) also calculate the threshold ionization needed for efficient MRI; they find it requires $\mathcal{X}_e > 10^{-13}$, less than our threshold of 10^{-11} , because they use a slightly different set of assumptions for the onset of MRI than we do.

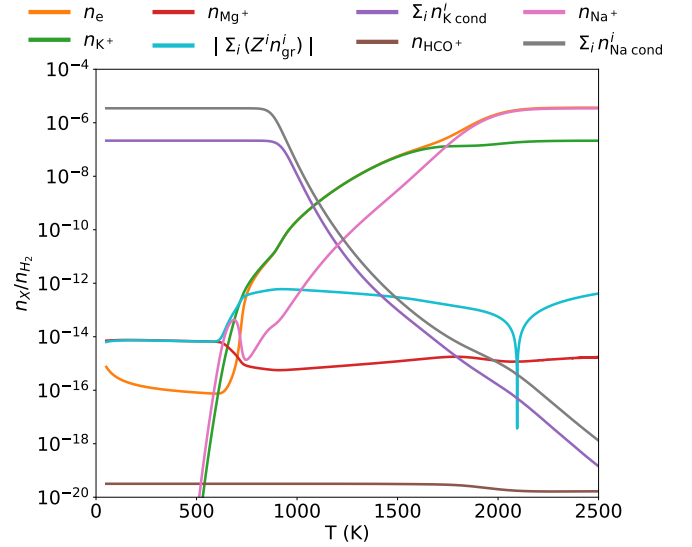


Figure B1. The ionization state of the reaction network including sodium is shown. The distribution is the fiducial MRN distribution with dust-to-gas ratio $f_{\text{dg}} = 0.01$, MRN exponent $q = 3.5$, $a_{\text{min}} = 10^{-5}$ cm, $a_{\text{max}} = 10^{-1}$ cm at $n_{\text{H}_2} = 10^{14} \text{ cm}^{-3}$.

APPENDIX C: LINEAR RELATIONSHIP BETWEEN GRAIN CHARGE AND GRAIN SIZE

Draine & Sutin (1987) (excluding the effects of ion and thermionic emission) considered a distribution of charges for each grain size, and determined that the distribution of charges on a single grain size follows a Gaussian, whose mean $Z^i \propto a^i$ (or equivalently $\tau^i \equiv a^i kT/e^2$). A derivation for this is provided in Okuzumi (2009). We provide a similar derivation here, with ion and thermionic emission included.

Consider the detailed balance equation between state Z^i and state $Z^i + 1$:

$$\begin{aligned}
 p(Z^i, \tau^i) & \left[n_{\text{m}^+} S_{\text{m}^+} v_{\text{m}^+} \bar{J}(Z^i, \tau^i) + n_{\text{M}^+} S_{\text{M}^+} v_{\text{M}^+} \bar{J}(Z^i, \tau^i) \right. \\
 & + n_{\text{K}^+} S_{\text{K}^+} v_{\text{K}^+} \bar{J}(Z^i, \tau^i) \\
 & \left. + 4\lambda_R \frac{4\pi m_e (kT)^2}{h^3} \exp(-W/kT) \exp(-Z^i/\tau^i) \right] \\
 & \approx p(Z^i + 1, \tau^i) \left[n_e S_e v_e \bar{J}(-Z^i, \tau^i) \right. \\
 & \left. + f_+(Z^i/\tau^i) n_{\text{K}^+} S_{\text{K}^+} v_{\text{K}^+} \bar{J}(Z^i, \tau^i) + f_+(Z^i/\tau^i) n_{\text{K}^0} S_{\text{K}^0} v_{\text{K}^0} \right], \quad (\text{C1})
 \end{aligned}$$

where S_x defines the sticking coefficient, and v_x the thermal velocity of species x . The probability that the grain with size τ^i will have charge Z^i is denoted $p(Z^i, \tau^i)$. This is not an exact equality, since the \bar{J} and f_+ terms on the right-hand side should be functions of $Z^i + 1$; however, provided these functions do not change significantly with small changes in Z , we can make this approximation. In the limit of large τ , this approximation is valid. We shall illustrate why the approximation is valid for f_+ . The derivative of equation (10) for f_+ with respect to Z^i is

$$\frac{\partial f_+^i}{\partial Z^i} = \frac{1}{\tau^i} (1 - f_+^i) f_+^i, \quad (\text{C2})$$

where $f_+^i < 1$, meaning that $\frac{\partial f_+^i}{\partial Z^i} \rightarrow 0$ in the limit of large τ^i .

For $\tau^i \gg 1$ and $|Z^i| \gg 1$, the focusing factor of species x is (Draine & Sutin 1987)

$$\bar{J}_x(Z^i e/q_x < 0) \rightarrow \left(1 - \frac{Z^i e}{q_x \tau^i}\right) \quad (\text{C3})$$

$$\bar{J}_x(Z^i e/q_x > 0) \rightarrow \exp\left(-\frac{Z^i e}{q_x \tau^i}\right), \quad (\text{C4})$$

where q_x is the charge of the species x interacting with the grain. Computing the derivatives with respect to Z^i , as we do in C2, it is trivial to show that these derivatives also vanish in the limit of large τ^i .

Okuzumi (2009) uses the assumption that $\langle (Z^i)^2 \rangle^{-\frac{1}{2}} \sim (\tau^i)^{-\frac{1}{2}} \sim \epsilon \ll 1$, the first relation is justified after deriving the form of $\langle (Z^i)^2 \rangle$. Using the additional assumption that $p(Z^i, \tau^i)$ varies on the scale of $\langle (Z^i)^2 \rangle^{\frac{1}{2}}$

$$p(Z^i + 1, \tau^i) = p(Z^i, \tau^i) + \frac{\partial p}{\partial Z^i}(Z^i, \tau^i) + \mathcal{O}(\epsilon^2) \quad (\text{C5})$$

Substituting this expansion into equation (C1), an analogous differential equation to that of Okuzumi (2009) is derived with

$$\frac{\partial p}{\partial Z^i}(Z^i, \tau^i) + W(Z^i, \tau^i)p(Z^i, \tau^i) \approx 0 \quad (\text{C6})$$

However, in this case $W(Z^i, \tau^i)$ is given by

$$W(Z^i, \tau^i) = 1 - \frac{\lambda_{\text{ions}} \left(1 - \frac{Z^i}{\tau^i}\right) + \alpha_{\text{therm}} \exp\left(-\frac{Z^i}{\tau^i}\right)}{\lambda_e \exp\left(\frac{Z^i}{\tau^i}\right) + \lambda_{\text{K}^+} \left(1 - \frac{Z^i}{\tau^i}\right) f_+^i + \lambda_{\text{K}^0} f_+^i} \quad (\text{C7})$$

where we have used $\lambda_x = n_x S_x v_x$, $\lambda_{\text{ions}} = \lambda_{\text{m}^+} + \lambda_{\text{M}^+} + \lambda_{\text{K}^+}$ and $\alpha_{\text{therm}} = 4\lambda_R \frac{4\pi m_e (kT)^2}{h^3} \exp(-W/kT)$ to simplify the notation. In the limit $kT \ll E_a < W$, we have

$$W(Z^i, \tau^i) = 1 - \frac{\lambda_{\text{ions}} \left(1 - \frac{Z^i}{\tau^i}\right)}{\lambda_e \exp\left(\frac{Z^i}{\tau^i}\right)} \quad (\text{C8})$$

which is the form in Okuzumi (2009), except allowing for the presence of multiple ions.

The grain charge Z_0^i with maximum probability, i.e., for which $\frac{\partial p}{\partial Z^i} = 0$, is found by determining the root $W(Z_0^i, \tau^i) = 0$ where W is given by equation (C7). Since $Z_0^i/\tau^i = \psi$ depends only on plasma quantities, all other grain sizes denoted by the superscript i have the same constant ψ . Therefore, $Z_0^i = \psi \tau^i$ for all i , and the root of only a single equation is required to determine the most probable grain charge for each grain size. For a Gaussian, the most probable grain charge for a single grain size Z_0^i is also the mean grain charge for that grain size \bar{Z}^i . For the single grain charge Z_{single}^i we have used for each grain size elsewhere in this work, we also determine the root $W(Z_{\text{single}}^i, \tau^i) = 0$, thus Z_{single}^i is the most probable grain size, and thus for a Gaussian distribution, the mean grain charge.

$W(Z^i, \tau^i)$ is then expanded about Z_0^i to first order in $|\delta Z^i|/\tau^i$. Since

$$\begin{aligned} \frac{\partial W}{\partial Z^i} &= \frac{1}{\lambda_e \exp\left(\frac{Z^i}{\tau^i}\right) + \lambda_{\text{K}^+} \left(1 - \frac{Z^i}{\tau^i}\right) f_+^i + \lambda_{\text{K}^0} f_+^i} \times \\ &\left[\lambda_{\text{ions}} + \alpha_{\text{therm}} \exp\left(-\frac{Z^i}{\tau^i}\right) + \lambda_e \exp\left(\frac{Z^i}{\tau^i}\right) - \lambda_{\text{K}^+} f_+^i \right. \\ &\quad \left. - \left(\lambda_{\text{K}^+} \left(1 - \frac{Z^i}{\tau^i}\right) + \lambda_{\text{K}^0} \right) f_+^i (f_+^i - 1) \right] \frac{1}{\tau^i} \quad (\text{C9}) \end{aligned}$$

$\frac{\partial^2 W}{\partial Z^i^2} \propto 1/(\tau^i)^2$ and $W(Z_0^i, \tau^i) = 0$, to first order in $|\delta Z^i|/\tau^i$,

$$\begin{aligned} W &\approx \frac{1}{\lambda_e \exp\left(\frac{Z_0^i}{\tau^i}\right) + \lambda_{\text{K}^+} \left(1 - \frac{Z_0^i}{\tau^i}\right) f_+^i + \lambda_{\text{K}^0} f_+^i} \times \\ &\left[\lambda_{\text{ions}} + \alpha_{\text{therm}} \exp\left(-\frac{Z_0^i}{\tau^i}\right) + \lambda_e \exp\left(\frac{Z_0^i}{\tau^i}\right) - \lambda_{\text{K}^+} f_+^i \right. \\ &\quad \left. - \left(\lambda_{\text{K}^+} \left(1 - \frac{Z_0^i}{\tau^i}\right) + \lambda_{\text{K}^0} \right) f_+^i (f_+^i - 1) \right] \frac{|\delta Z^i|}{\tau^i} \quad (\text{C10}) \end{aligned}$$

The expansion to first order in $|\delta Z^i| \ll \tau^i$ may be re-written in terms of the variance (which has yet to be determined) $|\delta Z^i| \ll \langle (Z^i)^2 \rangle^{\frac{1}{2}} (\tau^i)^{\frac{1}{2}}$. This implies that the expansion is valid provided $|\delta Z^i| \lesssim \langle (Z^i)^2 \rangle^{\frac{1}{2}}$.

Given this form of W , $p(Z^i, \tau^i)$ follows a Gaussian with a mean Z_0^i , with a variance $\langle (Z^i)^2 \rangle$, where

$$\begin{aligned} \langle (\Delta Z^i)^2 \rangle &\approx \left[\lambda_e \exp\left(\frac{Z_0^i}{\tau^i}\right) + \lambda_{\text{K}^+} \left(1 - \frac{Z_0^i}{\tau^i}\right) f_+^i + \lambda_{\text{K}^0} f_+^i \right] \times \\ &\left[\lambda_{\text{ions}} + \alpha_{\text{therm}} \exp\left(-\frac{Z_0^i}{\tau^i}\right) + \lambda_e \exp\left(\frac{Z_0^i}{\tau^i}\right) - \lambda_{\text{K}^+} f_+^i \right. \\ &\quad \left. - \left(\lambda_{\text{K}^+} \left(1 - \frac{Z_0^i}{\tau^i}\right) + \lambda_{\text{K}^0} \right) f_+^i (f_+^i - 1) \right]^{-1} \tau^i \quad (\text{C11}) \end{aligned}$$

To show that $\langle (\Delta Z^i)^2 \rangle$ is order τ^i , consider limiting values of Z_0^i/τ^i . In the limit $Z_0^i/\tau^i \gg 1$, $\langle (\Delta Z^i)^2 \rangle = \tau^i$ and for $Z_0^i/\tau^i \ll -1$, we also have $\langle (\Delta Z^i)^2 \rangle = \tau^i$. When $Z_0^i/\tau^i \rightarrow 0$, $\langle (\Delta Z^i)^2 \rangle \geq \frac{1}{2} \tau^i$.

We now plot a full distribution $p(Z^i, \tau^i)$ by using the recurrence relation equation (C1) and the normalization $\sum_Z p(Z^i, \tau^i) = 1$. We compute ψ and $\langle (\Delta Z^i)^2 \rangle$ according to the method described above and plot the resulting Gaussian alongside the full distribution. To verify the method, we compare the Gaussian derived in this work to the Gaussian found neglecting thermionic and ion emission in Draine & Sutin (1987) and Okuzumi (2009). For low temperatures $T \lesssim 500$ K, the Gaussians should be identical as emission processes are not active. We choose $T = 166$ K, for which $\tau^i = 1$ for our minimum grain size of 10^{-5} cm. In Fig. C1, we plot the distributions for $\tau^i = 1$ and $\tau^i = 10$, corresponding to 10^{-5} cm and 10^{-4} cm. We compute the chemical abundances (assuming a single grain charge for each grain size as in the rest of the work) at the fiducial $n_{\text{H}_2} = 10^{14} \text{ cm}^{-3}$, with the fiducial MRN distribution with parameters $q = 3.5$, $a_{\text{min}} = 10^{-5}$ cm and $a_{\text{max}} = 10^{-1}$ cm. From Fig. C1, we see that the distribution $p(Z^i, \tau^i)$ is fit well by both the full Gaussian and Gaussian excluding ion and thermionic emission due to Draine & Sutin (1987).

Finally, we investigate the fit of the Gaussian derived here to the full distribution $p(Z^i, \tau^i)$ at a temperature at which ion and thermionic emission are active. We choose $T = 1000$ K at the fiducial $n_{\text{H}_2} = 10^{14} \text{ cm}^{-3}$, with the fiducial MRN distribution with parameters $q = 3.5$, $a_{\text{min}} = 10^{-5}$ cm and $a_{\text{max}} = 10^{-1}$ cm. We plot the distributions $p(Z^i, \tau^i)$ along with the Gaussian approximations for $\tau = 6$ and $\tau = 60$, corresponding again to 10^{-5} cm and 10^{-4} cm, in Fig. C2. We see that a Gaussian provides a good approximation to the distributions.

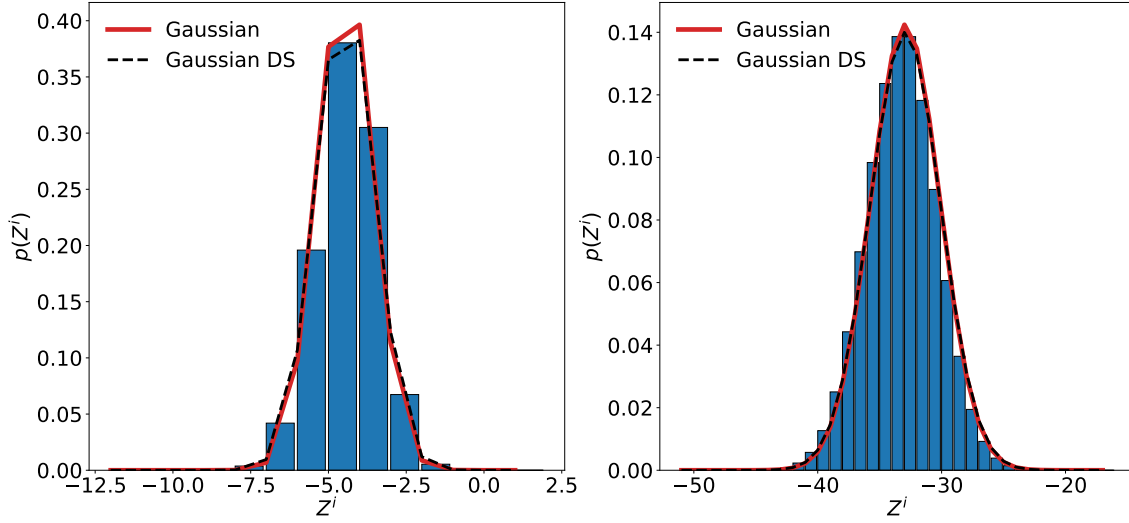


Figure C1. Distributions of $p(Z^i)$ computed at $T = 166$ K. Chemical abundances are computed with our network (using a single charge for each grain size) at the same temperature, with $n_{\text{H}_2} = 10^{14} \text{ cm}^{-3}$, a fiducial MRN distribution with parameters $q = 3.5$, $a_{\text{min}} = 10^{-5}$ cm and $a_{\text{max}} = 10^{-1}$ cm. The distribution $p(Z^i)$ is plotted for two separate grain sizes 10^{-5} cm (left) and 10^{-4} cm (right), corresponding to $\tau = 1$ and $\tau = 10$ respectively. Overplotted are the Gaussians computed including thermionic and ion emission (red; N.B. these effects are insignificant at this temperature), and the Gaussian due to [Draine & Sutin \(1987\)](#) (black, dashed), which does not include these effects. The distribution is well fit by a Gaussian, and agreement can be seen between both Gaussians, as expected.

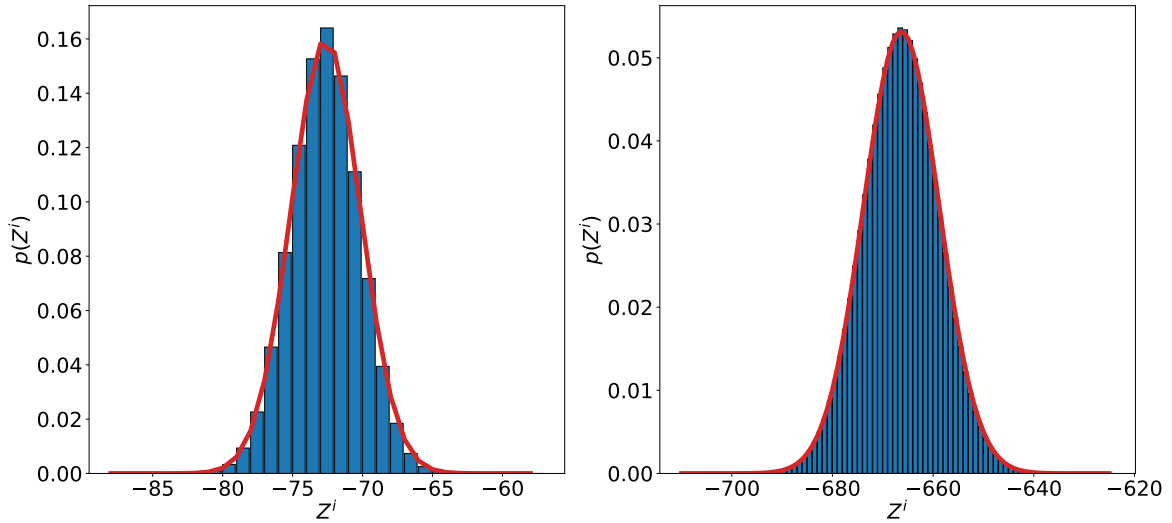


Figure C2. Distributions of $p(Z^i)$ computed at $T = 1000$ K. Chemical abundances are computed with our network (using a single charge for each grain size) at the same temperature, with $n_{\text{H}_2} = 10^{14} \text{ cm}^{-3}$, a fiducial MRN distribution with parameters $q = 3.5$, $a_{\text{min}} = 10^{-5}$ cm and $a_{\text{max}} = 10^{-1}$ cm. The distribution $p(Z^i)$ is plotted for two separate grain sizes 10^{-5} cm (left) and 10^{-4} cm (right), corresponding to $\tau = 6$ and $\tau = 60$ respectively. The Gaussian computed in this work, including thermionic and ion emission, is overplotted (red). The distributions $p(Z^i)$ are well fit by the Gaussian.

APPENDIX D: COMPARISON WITH EFFECTIVE DUST-TO-GAS RATIO

Neglecting the effect of grain charge, the total grain surface area determines the chemistry, i.e., any two grain size distributions with

the same total surface area produce the same abundances. To explore the general case of charged grains, [Bai & Goodman \(2009\)](#) used a network specialized to the cooler regions of the disc (i.e., no significant thermal ionization) with two grain sizes. They included charge transfer between grains and found it to be negligible, thus the two

grain populations act independently of one another. They found that the abundance of free electrons was controlled by $\sum f_{\text{dg}}^i(a^i)/(a^i)^p$ with a controlling p between 1 and 2. Since the dust-to-gas ratio scales as a^3 , $p = 1$ corresponds to keeping a fixed total grain surface area, the naïve expectation.

Adding to this work for the high-temperature network of [De-sch & Turner \(2015\)](#), [Jankovic et al. \(2021\)](#) found that above a certain temperature ($T \gtrsim 1000$ K), the controlling parameter for the electron number density was $p = 1.5$. For a whole population of grain sizes, and an arbitrarily chosen single effective grain size a_{eff} , they thus used an effective dust-to-gas ratio $f_{\text{dg, eff}} = a_{\text{eff}}^p \int_{a_{\text{min}}}^{a_{\text{max}}} dn(a)m(a)/(\rho_{gr}a^p)$ with $p = 1.5$, that would produce the same electron abundance as the distribution as a whole.

Our model, which includes *exactly* the effect of a distribution of grain sizes, is compared with the [Jankovic et al. \(2021\)](#) model in [Fig. D1](#) for a range of dust-to-gas ratios (f_{dg}) and MRN power-law indices (q).

At low temperatures, where non-thermal ionization dominates, an effective dust-to-gas ratio with $p = 1.5$ does not yield accurate gas-phase (or grain-phase) abundances. This had been previously demonstrated by [Jankovic et al. \(2021\)](#).

At high temperatures ($T \gtrsim 1000$ K), the effective dust-to-gas ratio calculation accurately reproduces the dominant gas-phase abundances; therefore, if one only wanted to compute resistivities at these temperatures, an effective dust-to-gas ratio calculation with $p = 1.5$ would be valid.

However, when grains are not one of the dominant charged species, the grain charge can be quite inaccurate. This is particularly evident for the distributions with $q = 2.0$, where the fractional error on the effective dust-to-gas ratio calculation is significant. This would considerably alter the collision cross-sections that grains present to one another, as well as the impact velocities of these collisions. Therefore, if one wanted to study the collisional evolution of the grains, an effective dust-to-gas ratio cannot safely be used.

This paper has been typeset from a $\text{\TeX}/\text{\LaTeX}$ file prepared by the author.

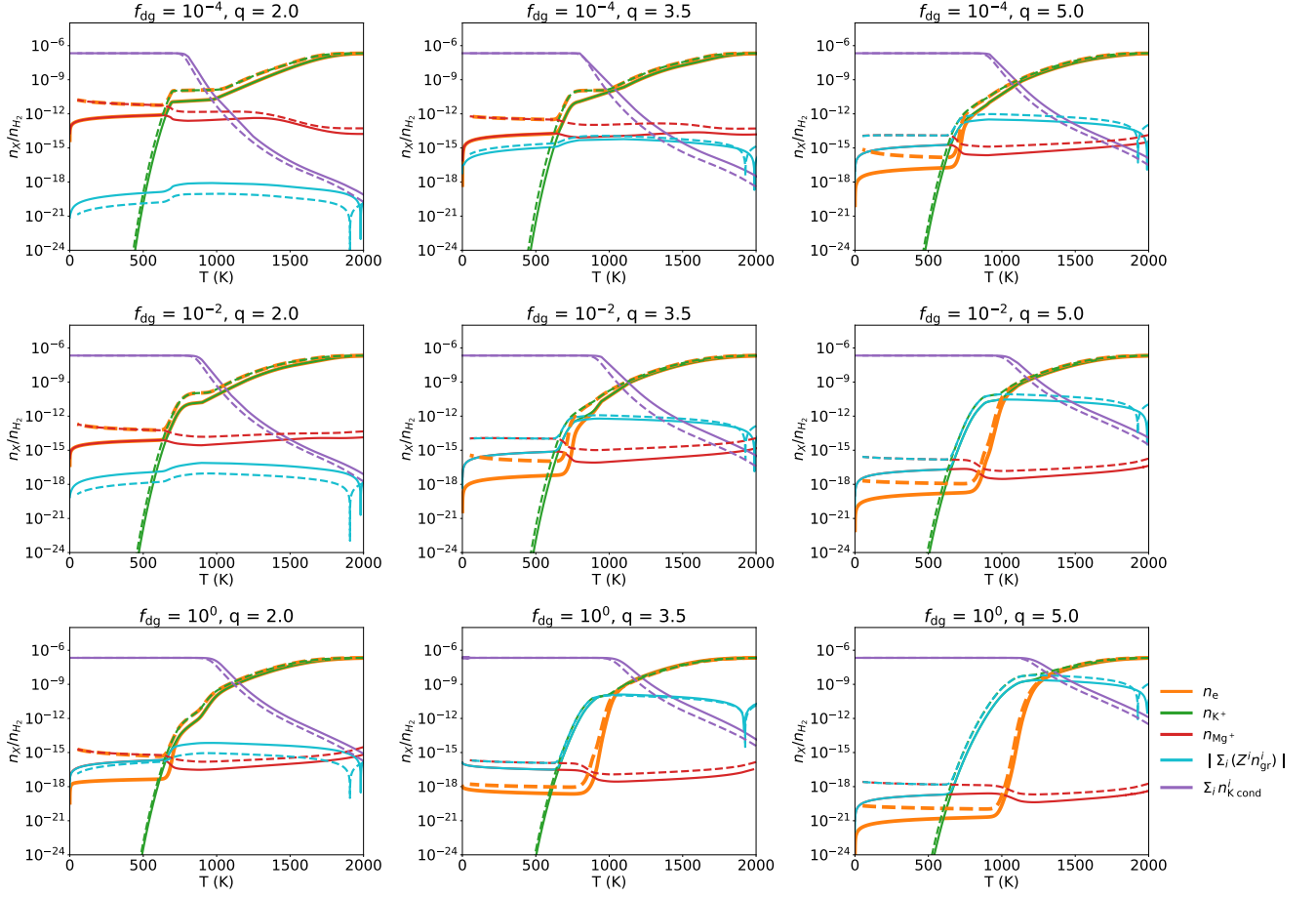


Figure D1. The ionization state of the reaction network is shown for grains following an MRN distribution for a grid of dust-to-gas ratio f_{dg} and MRN exponent values q . The exact model for a distribution of grain sizes is shown in solid lines, while the effective method for modelling a distribution of grain sizes is shown in dashed lines. The remaining parameters used are the fiducial $a_{\min} = 10^{-5}$ cm, $a_{\max} = 10^{-1}$ cm at $n_{\text{H}_2} = 10^{14}$ cm $^{-3}$. The thickness of the lines for n_e have been increased to show where they have gone behind other lines.